Comput Geosci (2015) 19:233–256
DOI 10.1007/s10596-014-9462-7

ORIGINAL PAPER

On an inverse source problem for enhanced oil recovery by wave motion maximization in reservoirs

Pranav M. Karve · Sezgin Kucukcoban · Loukas F. Kallivokas

Received: 10 July 2014 / Accepted: 11 December 2014 / Published online: 28 December 2014

Abstract We discuss an optimization methodology for focusing wave energy to subterranean formations using strong motion actuators placed on the ground surface. The motivation stems from the desire to increase the mobility of otherwise entrapped oil. The goal is to arrive at the spatial and temporal description of surface sources that are capable of maximizing mobility in the target reservoir. The focusing problem is posed as an inverse source problem. The underlying wave propagation problems are abstracted in two spatial dimensions, and the semi-infinite extent of the physical domain is negotiated by a buffer of perfectly-matched-layers (PMLs) placed at the domain's truncation boundary. We discuss two possible numerical implementations: Their utility for deciding the tempo-spatial characteristics of optimal wave sources is shown via numerical experiments. Overall, the simulations demonstrate the inverse source method's ability to simultaneously optimize load locations and time signals leading to the maximization of energy delivery to a target formation.

Keywords Inverse source problem · Enhanced oil recovery · PDE-constrained optimization · Elastic wave energy focusing

P. M. Karve · L. F. Kallivokas (✉)
Department of Civil, Architectural and Environmental Engineering, The University of Texas at Austin,
301 East Dean Keeton St. Stop C1747,
Austin, TX 78712, USA
e-mail: loukas@mail.utexas.edu

S. Kucukcoban
Stress Engineering Services Inc., 13610 Westland East Blvd. Building 2, Houston, TX 77041, USA

1 Introduction

Elastic wave stimulation of oil reservoirs has been suggested as a viable recourse for the purpose of enhanced oil recovery (EOR) [3, 4, 6, 10, 12, 16]. Seismic EOR, as it is sometimes referred to, relies on the ability of propagating waves, generated by sources placed on or below the ground surface, to mobilize trapped oil particles. Laboratory and field experiments [4] suggest that such mobilization is possible either by dislodgement into the fluid flow of the oil particles adhering to the pore wall [12] or by the release of trapped oil-blobs from the pores due to a Haines jump-like phenomenon [2, 3, 6]. After the droplets are dislodged, conventional methods can be used for recovery. In general, wave-based EOR methods are economically competitive and do not suffer from low sweep efficiency problems in heterogeneous reservoirs when compared to other EOR methods [10, 14].

From a technical perspective, uniform, or as uniform as possible, illumination of the reservoir by a sufficiently strong wave field is essential to the success of wave-based EOR methods. Radiation damping, intrinsic, and apparent attenuation present challenges in the field implementation of any wave-based EOR process. Although the dissipative character of the problem cannot be altered, intelligent choices for the locations and frequency content of the wave sources can help maximize reservoir shaking. For example, wave sources operating at certain amplification frequencies (characteristic of the reservoir and its surroundings) have been shown to produce stronger wave motion in the targeted formations [10] than blind sources operating at arbitrarily selected frequencies. It can also be argued that if the sources are situated and synchronized in a manner that promotes

constructive interference at the target formation, then sufficiently strong motion may result despite the attenuation. In this article, we discuss a systematic methodology for making a judicious choice about both the placement and the frequency content of wave sources used for focusing wave energy to subsurface formations.

Frequency sweep is one possibility for determining the optimal (monochromatic) frequency of a ground motion actuator at which the oil mobility in the formation will be maximized. When given the location and strength of the wave sources, the frequency sweep relies on a linear elastodynamic or poroelastodynamic model for capturing the relevant physics and for determining the strength of the wave field within the reservoir over the driving frequency range of interest. Although traversing the frequency spectrum with fixed load locations is a computationally manageable task, an exhaustive search for the optimal load locations that could potentially maximize mobility is computationally prohibitive. This shortcoming of the frequency sweep approach could be overcome if the problem were formulated in terms of a *search* for the *optimal* source characteristics, both spatial and temporal, which, in turn, calls for casting the search as an inverse source problem.

The inverse source problem approach for the maximization of motion in a target formation is akin to the inverse medium problem typically arising in exploration geophysics [1, 5, 7, 11, 18], where subsurface imaging relies on the minimization of the difference between experimentally collected and computationally obtained data. Similarly, the inverse source problem is formulated as a constrained optimization problem, where minimization of an appropriate objective functional is tantamount to the maximization of wave motion in the reservoir. The search for optimal source characteristics is carried out by staying within the constraints of the governing physics and of equipment limitations.

Schematically, the inversion procedure is depicted in Fig. 1. The procedure is initialized with the definition of the motion metric in the objective functional ($\mathcal{L}$) and with initial guesses for the source characteristics, i.e., for the source location and the associated time signals (*control variables*). Following a constrained optimization approach, whereby the governing IBVP is side-imposed to $\mathcal{L}$, the first-order optimality conditions typically lead to a triad of forward, adjoint, and control problems (box A, Fig. 1). The wave source characteristics are updated, following, for example, a gradient-based scheme, which requires computation of the functional's gradients in the space of the source characteristics. Thus, in general, the numerical solution of the inverse source problem performs two key operations: optimization (minimization) in the space of the control variables and discretization of the ensuing triad of BVPs. These operations can be performed in different order and would yield different gradients of the objective functional in question. Depending on the operational order, there arises either an *optimize-then-discretize* (OTD) or a *discretize-then-optimize* (DTO) approach; they are both shown in Fig. 2 [8, 15].

Either of the two approaches can be used to solve an inverse source problem aimed at the maximization of wave motion within a reservoir. For example, in Jeong et al. [9,

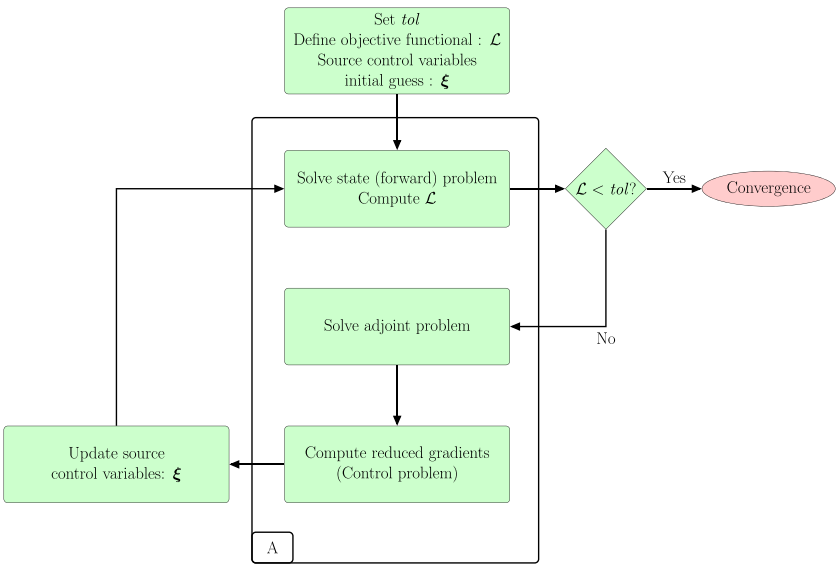

Fig. 1 General framework of the inverse source process

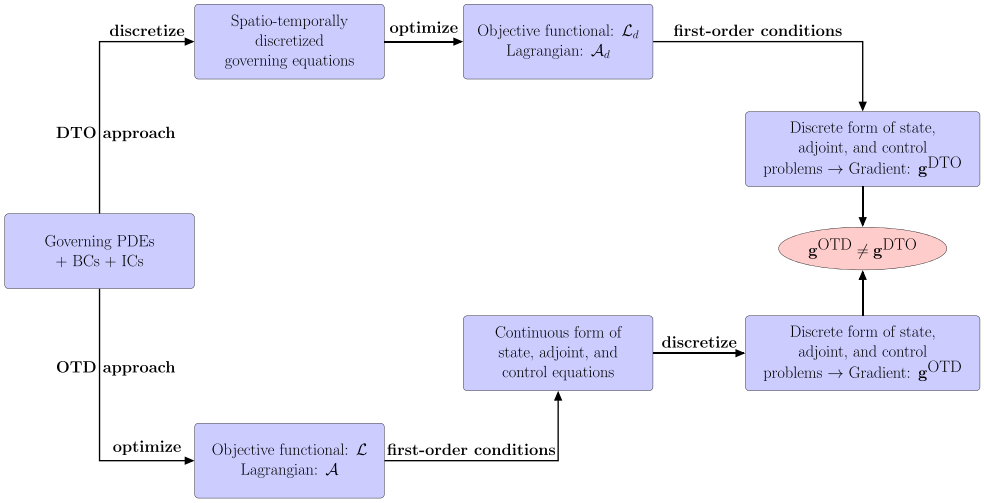

Fig. 2 Candidate algorithms for the core optimization scheme depicted in box A of Fig. 1

10], the OTD approach was used for optimizing the frequency content of surface sources used in wave-based EOR for reservoirs abstracted in one or two spatial dimensions, where, however, the load locations were treated as fixed.

In this article, we adopt a similar two-dimensional elastic setting for optimizing the wave source characteristics, but seek to optimize both the source frequency content (or time signal) and the source locations. The reservoir is represented by a target inclusion within an arbitrarily heterogeneous geological formation. We utilize hybrid perfectly-matched-layers (PMLs) [13] to truncate the physical domain of interest. We discuss the formulation and implementation of both the OTD and the DTO approaches and conduct numerical experiments. We compare the performance of the frequency sweep approach with that of the inverse source problem approach and show that simultaneous optimization with respect to both source locations and time signals is important for a higher energy yield. We also discuss the effect of polarization of the applied surface tractions on the efficiency of energy focusing and report results attesting to the ability of the inverse source approach to prescribe wave sources that could improve the mobility of a reservoir's bypassed oil.

2 The forward problem

Our working hypothesis is that the material properties of the targeted geostructure and those of the surrounding formations are known *a priori*. For example, if Ω_a in Fig. 3 is the target reservoir, then the properties of both Ω_a and its surrounding formations Ω_{reg} are considered known. The forward problem consists of finding the displacement field (velocity and acceleration) in the domain of interest, given suitable boundary and initial conditions, which include the applied surface tractions. We discuss next the elements of the forward problem.

2.1 Strong form

We are concerned with elastic wave propagation in a two-dimensional (2D) heterogeneous, elastic halfspace. We intend to use finite elements for the numerical solution of

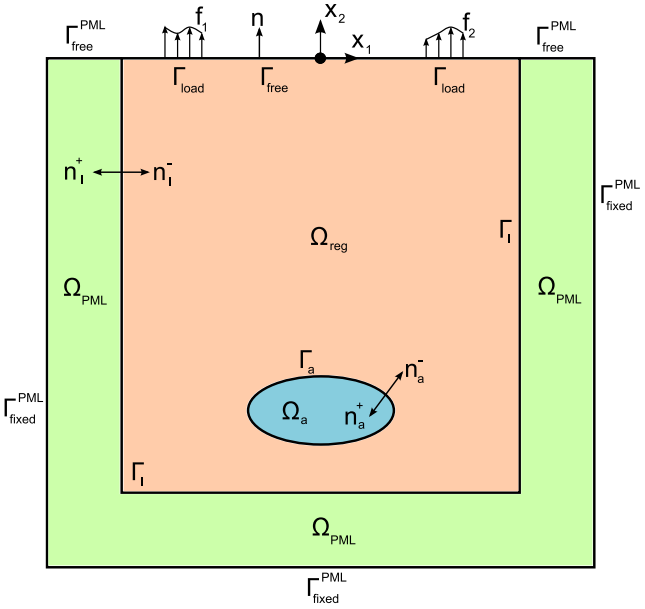

Fig. 3 Problem definition

the BVPs. This choice, in turn, necessitates the truncation of the semi-infinite domain. We use hybrid perfectly-matched-layers (PMLs)[13] to realize a physically faithful simulation of wave propagation within the computational domain. Figure 3 shows the truncated 2D elastic domain Ω_{reg} that has been augmented with PMLs (Ω_{PML}). Ω_{reg} envelops the target inclusion Ω_{a}. $\mathbf{u}_{\text{a}}(\mathbf{x}, t)$ represents the displacement field in the target inclusion (Ω_{a}), whereas $\mathbf{u}_{\text{b}}(\mathbf{x}, t)$ denotes the displacement in the rest of the domain ($\Omega_{\text{reg}} \cup \Omega_{\text{PML}}$). The governing equations in $\Omega = \Omega_{\text{a}} \cup \Omega_{\text{reg}} \cup \Omega_{\text{PML}}$, for time $t \in (0, T] = \mathsf{J}$, are given as :

$$\mathbf{div}\left[\mu_{\text{a}}\left(\nabla\mathbf{u}_{\text{a}} + \nabla\mathbf{u}_{\text{a}}^T\right)\right] + \mathbf{div}\left[\{\lambda_{\text{a}}\ \text{div}\ \mathbf{u}_{\text{a}}\}\,\mathbf{I}\right] - \rho_{\text{a}}\ddot{\mathbf{u}}_{\text{a}} = \mathbf{0},\ \mathbf{x} \in \Omega_{\text{a}}, \tag{1}$$

and

$$\mathbf{div}\left[\mu_{\text{b}}\left(\nabla\mathbf{u}_{\text{b}} + \nabla\mathbf{u}_{\text{b}}^T\right)\right] + \mathbf{div}\left[\{\lambda_{\text{b}}\,\text{div}\,\mathbf{u}_{\text{b}}\}\,\mathbf{I}\right] - \rho_{\text{b}}\ddot{\mathbf{u}}_{\text{b}} = \mathbf{0},\ \mathbf{x} \in \Omega_{\text{reg}}, \tag{2a}$$

$$\mathbf{div}\left(\dot{\mathbf{S}}^T\tilde{\Lambda}_e + \mathbf{S}^T\tilde{\Lambda}_p\right) - \rho_{\text{b}}\left(\mathsf{a}\ddot{\mathbf{u}}_{\text{b}} + \mathsf{b}\dot{\mathbf{u}}_{\text{b}} + \mathsf{c}\mathbf{u}_{\text{b}}\right) = \mathbf{0},\ \mathbf{x} \in \Omega_{\text{PML}}, \tag{2b}$$

$$\mathcal{D} : \left(\mathsf{a}\ddot{\mathbf{S}} + \mathsf{b}\dot{\mathbf{S}} + \mathsf{c}\mathbf{S}\right) - \frac{1}{2}\left[\nabla\mathbf{u}_{\text{b}}\tilde{\Lambda}_p + \tilde{\Lambda}_p(\nabla\mathbf{u}_{\text{b}})^T + \nabla\dot{\mathbf{u}}_{\text{b}}\tilde{\Lambda}_e + \tilde{\Lambda}_e(\nabla\dot{\mathbf{u}}_{\text{b}})^T\right] = \mathbf{0},\quad \mathbf{x} \in \Omega_{\text{PML}}, \tag{2c}$$

where an overdot ($\dot{}$) denotes a derivative with respect to time and a colon (:) represents tensor inner product. Equations 1 and 2 are the elastodynamics equations for a semi-infinite medium, augmented by PMLs [13]. $\mathbf{S}(\mathbf{x}, t)$ is the stress *history* tensor, given by,

$$\mathbf{S}(\mathbf{x}, t) = \begin{bmatrix} \mathbf{S}_{11}(\mathbf{x}, t) & \mathbf{S}_{12}(\mathbf{x}, t) \\ \mathbf{S}_{21}(\mathbf{x}, t) & \mathbf{S}_{22}(\mathbf{x}, t) \end{bmatrix} = \int_0^t \boldsymbol{\sigma}(\mathbf{x}, \tau)d\tau, \tag{3}$$

where $\boldsymbol{\sigma}$ is the Cauchy stress tensor. $\tilde{\Lambda}_e$ and $\tilde{\Lambda}_p$ are components of the stretching tensor, and $\mathsf{a}, \mathsf{b}, \mathsf{c}$ are coefficients defining coordinate stretching in the PML region. Their detailed definitions are beyond the scope of this article and can be found in [13]. $(\lambda_{\text{a}}, \mu_{\text{a}}, \rho_{\text{a}})$ and $(\lambda_{\text{b}}, \mu_{\text{b}}, \rho_{\text{b}})$ are the Lamé parameters and mass density for the inclusion Ω_{a} and $\Omega_{\text{reg}} \cup \Omega_{\text{PML}}$, respectively. $\mathcal{D}$ is the compliance tensor, so that the constitutive law takes the form $\mathcal{D} : \dot{\mathbf{S}} = \frac{1}{2}(\nabla\mathbf{u}_{\text{b}} + \nabla\mathbf{u}_{\text{b}}^T)$. For $t \in \mathsf{J}$, the governing equations are subjected to the following boundary conditions:

$$\mathbf{u}_{\text{b}}(\mathbf{x}, t) = \mathbf{0},\ \mathbf{x} \in \Gamma_{\text{fixed}}^{\text{PML}}, \tag{4a}$$

$$\left[\mu_{\text{b}}\left(\nabla\mathbf{u}_{\text{b}} + \nabla\mathbf{u}_{\text{b}}^T\right) + \{\lambda_{\text{b}}\ \text{div}\ \mathbf{u}_{\text{b}}\}\,\mathbf{I}\right]\mathbf{n} = \mathbf{f}(\mathbf{x}, t),\ \mathbf{x} \in \Gamma_{\text{load}}, \tag{4b}$$

$$\left[\mu_{\text{b}}\left(\nabla\mathbf{u}_{\text{b}} + \nabla\mathbf{u}_{\text{b}}^T\right) + \{\lambda_{\text{b}}\ \text{div}\ \mathbf{u}_{\text{b}}\}\,\mathbf{I}\right]\mathbf{n} = \mathbf{0},\ \mathbf{x} \in \Gamma_{\text{free}}, \tag{4c}$$

$$\left(\dot{\mathbf{S}}^T\tilde{\Lambda}_e + \mathbf{S}^T\tilde{\Lambda}_p\right)\mathbf{n} = \mathbf{0},\ \mathbf{x} \in \Gamma_{\text{free}}^{\text{PML}}; \tag{4d}$$

interface conditions :

$$\mathbf{u}_{\text{b}}^+ = \mathbf{u}_{\text{b}}^-,\ \mathbf{x} \in \Gamma_{\text{I}}, \tag{5a}$$

$$\left[\mu_{\text{b}}\left(\nabla\mathbf{u}_{\text{b}} + \nabla\mathbf{u}_{\text{b}}^T\right) + \{\lambda_{\text{b}}\ \text{div}\ \mathbf{u}_{\text{b}}\}\,\mathbf{I}\right]\mathbf{n}_{\text{I}}^+ = -\left(\dot{\mathbf{S}}^T\tilde{\Lambda}_e + \mathbf{S}^T\tilde{\Lambda}_p\right)\mathbf{n}_{\text{I}}^-,\ \mathbf{x} \in \Gamma_{\text{I}}, \tag{5b}$$

$$\mathbf{u}_{\text{a}}(\mathbf{x}, t) = \mathbf{u}_{\text{b}}(\mathbf{x}, t),\quad \mathbf{x} \in \Gamma_{\text{a}}, \tag{5c}$$

$$\boldsymbol{\sigma}_{\text{a}}(\mathbf{x}, t)^T\mathbf{n}_{\text{a}}^- = -\boldsymbol{\sigma}_{\text{b}}(\mathbf{x}, t)^T\mathbf{n}_{\text{a}}^+,\quad \mathbf{x} \in \Gamma_{\text{a}}; \tag{5d}$$

where

$$\boldsymbol{\sigma}_{\text{a}}(\mathbf{x}, t) = \mu_{\text{a}}\left(\nabla\mathbf{u}_{\text{a}} + \nabla\mathbf{u}_{\text{a}}^T\right) + \lambda_{\text{a}}(\text{div}\ \mathbf{u}_{\text{a}})\mathbf{I}, \tag{5e}$$

$$\boldsymbol{\sigma}_{\text{b}}(\mathbf{x}, t) = \mu_{\text{b}}\left(\nabla\mathbf{u}_{\text{b}} + \nabla\mathbf{u}_{\text{b}}^T\right) + \lambda_{\text{b}}(\text{div}\ \mathbf{u}_{\text{b}})\mathbf{I}; \tag{5f}$$

and initial conditions :

$$\mathbf{u}_{\text{a}}(\mathbf{x}, 0) = \mathbf{0},\quad \dot{\mathbf{u}}_{\text{a}}(\mathbf{x}, 0) = \mathbf{0},\quad \mathbf{x} \in \Omega_{\text{a}}, \tag{6a}$$

$$\mathbf{u}_{\text{b}}(\mathbf{x}, 0) = \mathbf{0},\quad \dot{\mathbf{u}}_{\text{b}}(\mathbf{x}, 0) = \mathbf{0},\quad \mathbf{x} \in \Omega_{\text{reg}} \cup \Omega_{\text{PML}}, \tag{6b}$$

$$\mathbf{S}(\mathbf{x}, 0) = \mathbf{0},\quad \dot{\mathbf{S}}(\mathbf{x}, 0) = \mathbf{0},\quad \mathbf{x} \in \Omega_{\text{PML}}. \tag{6c}$$

The *strong form* of the forward problem can be stated as: given loads $\mathbf{f}(\mathbf{x}, t)$, find $\mathbf{u}_{\text{a}} \in \mathbf{H}^1(\Omega_{\text{a}}) \times \mathsf{J}$, $\mathbf{u}_{\text{b}} \in \mathbf{H}^1(\Omega_{\text{reg}} \cup \Omega_{\text{PML}}) \times \mathsf{J}$, and $\mathbf{S} \in \mathcal{L}^2(\Omega_{\text{PML}}) \times \mathsf{J}$, so that they satisfy Eqs. 1 and 2 and conditions (4)–(6), where the pertinent function spaces for a scalar f, vector $\mathbf{u}$, and tensor $\mathbf{T}$ are given by:

$$L^2(\Omega) = \{f : \int_\Omega |f|^2 d\Omega < \infty\}, \tag{7a}$$

$$\mathcal{L}^2(\Omega) = \{\mathbf{T} : \mathbf{T} \in (L^2(\Omega))^{2\times 2}\}, \tag{7b}$$

$$H^1(\Omega) = \{f : \int_\Omega (|f|^2 + |\nabla f|^2)d\Omega < \infty,\ f(\mathbf{x}) = 0 \text{ if } \mathbf{x} \in \Gamma_{\text{fixed}}^{\text{PML}}\}, \tag{7c}$$

$$\mathbf{H}^1(\Omega) = \{\mathbf{u} : \mathbf{u} \in (H^1(\Omega))^2\}. \tag{7d}$$

2.2 Weak form

Next, we cast the forward problem in its weak form in the Galerkin sense. We multiply (1) by a vector test function $\mathbf{v}_{\text{a}}$, multiply (2a), (2b) by a vector test function $\mathbf{v}_{\text{b}}$, integrate by parts on their corresponding domains, and add them. Similarly, we multiply (2c) with tensor test function $\mathbf{T}$ and

integrate over Ω_{PML}. After some simplifications, using the boundary conditions (4) and interface conditions (5), we arrive at the following weak form:

$$\begin{aligned}
&\int_{\Omega_a}\Big\{\nabla\mathbf{v}_a : \Big[\mu_a\,(\nabla\mathbf{u}_a + \nabla\mathbf{u}_a^T) + \lambda_a\,(\text{div}\,\mathbf{u}_a)\mathbf{I}\Big] \\
&\qquad +\mathbf{v}_a\cdot\rho_a\ddot{\mathbf{u}}_a\Big\}\,d\Omega \\
&+\int_{\Omega_{\text{reg}}}\Big\{\nabla\mathbf{v}_b : \Big[\mu_b(\nabla\mathbf{u}_b + \nabla\mathbf{u}_b^T) + \lambda_b\,(\text{div}\,\mathbf{u}_b)\mathbf{I}\Big] \\
&\qquad +\mathbf{v}_b\cdot\rho_b\ddot{\mathbf{u}}_b\Big\}\,d\Omega \\
&+\int_{\Omega_{\text{PML}}}\Big\{\nabla\mathbf{v}_b : \Big(\dot{\mathbf{S}}^T\tilde{\Lambda}_e + \mathbf{S}^T\tilde{\Lambda}_p\Big) \\
&+\mathbf{v}_b\cdot\rho_b\,(a\ddot{\mathbf{u}}_b + b\dot{\mathbf{u}}_b + c\mathbf{u}_b)\Big\}\,d\Omega = \int_{\Gamma_{\text{load}}}\mathbf{v}_b\cdot\mathbf{f}\,d\Gamma, \qquad (8a)\\
&\int_{\Omega_{\text{PML}}}\mathbf{T} : \Big\{\mathcal{D} : (a\ddot{\mathbf{S}} + b\dot{\mathbf{S}} + c\dot{\mathbf{S}}) - \frac{1}{2}\Big[\nabla\mathbf{u}_b\tilde{\Lambda}_p \\
&+\tilde{\Lambda}_p(\nabla\mathbf{u}_b)^T + \nabla\dot{\mathbf{u}}_b\tilde{\Lambda}_e + \tilde{\Lambda}_e(\nabla\dot{\mathbf{u}}_b)^T\Big]\Big\}\,d\Omega = 0. \qquad (8b)
\end{aligned}$$

2.3 Semi-discrete form

Numerical solution of the forward problem requires discretization in space and time. We introduce spatial approximations via shape functions $\Phi(\mathbf{x}) \in \mathbf{H}_h^1(\Omega)$ and $\Psi(\mathbf{x}) \in \mathcal{L}_h^2(\Omega_{\text{PML}})$. Thus, the trial and test functions can be expressed as,

$$\begin{aligned}
\mathbf{v}_a &= \begin{bmatrix}\mathbf{v}_{a_1}^T\Phi(\mathbf{x})\\ \mathbf{v}_{a_2}^T\Phi(\mathbf{x})\end{bmatrix}, \qquad \mathbf{u}_a = \begin{bmatrix}\Phi(\mathbf{x})^T\widetilde{\mathbf{u}}_{a_1}(t)\\ \Phi(\mathbf{x})^T\widetilde{\mathbf{u}}_{a_2}(t)\end{bmatrix},\\
\mathbf{v}_b &= \begin{bmatrix}\mathbf{v}_{b_1}^T\Phi(\mathbf{x})\\ \mathbf{v}_{b_2}^T\Phi(\mathbf{x})\end{bmatrix}, \qquad \mathbf{u}_b = \begin{bmatrix}\Phi(\mathbf{x})^T\widetilde{\mathbf{u}}_{b_1}(t)\\ \Phi(\mathbf{x})^T\widetilde{\mathbf{u}}_{b_2}(t)\end{bmatrix}, \qquad (9a)
\end{aligned}$$

$$\begin{aligned}
\mathbf{T} &= \begin{bmatrix}\mathbf{T}_{11}^T\Psi(\mathbf{x}) & \mathbf{T}_{12}^T\Psi(\mathbf{x})\\ \mathbf{T}_{21}^T\Psi(\mathbf{x}) & \mathbf{T}_{22}^T\Psi(\mathbf{x})\end{bmatrix},\\
\mathbf{S} &= \begin{bmatrix}\Psi(\mathbf{x})^T\widetilde{\mathbf{S}}_{11}(t) & \Psi(\mathbf{x})^T\widetilde{\mathbf{S}}_{12}(t)\\ \Psi(\mathbf{x})^T\widetilde{\mathbf{S}}_{21}(t) & \Psi(\mathbf{x})^T\widetilde{\mathbf{S}}_{22}(t)\end{bmatrix}, \qquad (9b)
\end{aligned}$$

where, henceforth, quantities with a tilde over the quantity symbol $\widetilde{()}$ denote vectors of nodal values of the subtended quantity. Introducing Eq. 9 into Eqs. 8a and 8b yields the following semi-discrete equation:

$$\mathbf{M}\ddot{\mathbf{d}} + \mathbf{C}\dot{\mathbf{d}} + \mathbf{K}\mathbf{d} = \mathbf{F}, \qquad (10)$$

where,

$$\mathbf{d} = \Big[\widetilde{\mathbf{u}}_{a_1}\ \widetilde{\mathbf{u}}_{a_2}\mid \widetilde{\mathbf{u}}_{b_1}^{\text{reg}}\ \widetilde{\mathbf{u}}_{b_2}^{\text{reg}}\mid \widetilde{\mathbf{u}}_{b_1}^{\text{PML}}\ \widetilde{\mathbf{u}}_{b_2}^{\text{PML}}\ \widetilde{\mathbf{S}}_{11}\ \widetilde{\mathbf{S}}_{22}\ \widetilde{\mathbf{S}}_{12}\Big]^T, \qquad (11)$$

$$\mathbf{F} = \Big[\mathbf{0}\ \mathbf{0}\mid \mathbf{F}^1\ \mathbf{F}^2\mid \mathbf{0}\ \mathbf{0}\ \mathbf{0}\ \mathbf{0}\ \mathbf{0}\Big]^T. \qquad (12)$$

We note that $\mathbf{M}, \mathbf{C}$, and $\mathbf{K}$ are the global mass, damping, and stiffness matrices, respectively, $\mathbf{d}$ is the vector of unknown displacements (everywhere) and stress histories (PML only), and $\mathbf{F}$ is the force vector. The definitions of the element matrices used in our formulation are given in Appendix A. Further details of the global and element matrices can be found in [13].

2.4 Time integration

The time line is now discretized using a timestep Δt. We define the vector $\mathbf{d}_i = \mathbf{d}$, at time $t = i\,\Delta t$. The equation of motion of the spatio-temporally discretized system at time $t = (i+1)\Delta t$ can be written as,

$$\mathbf{M}\ddot{\mathbf{d}}_{i+1} + \mathbf{C}\dot{\mathbf{d}}_{i+1} + \mathbf{K}\mathbf{d}_{i+1} = \mathbf{F}_{i+1}. \qquad (13)$$

We employ Newmark's time integration scheme to integrate Eq. 13 in time. At time $t = 0$:

$$\mathbf{M}\ddot{\mathbf{d}}_0 = \mathbf{F}_0 - \mathbf{C}\dot{\mathbf{d}}_0 - \mathbf{K}\mathbf{d}_0, \qquad (14)$$

where $\mathbf{d}_0$ and $\dot{\mathbf{d}}_0$ are the prescribed displacement and velocity vectors. For any time $t \in \text{J}$, i.e., for $i \geq 0$, we calculate the acceleration $(\ddot{\mathbf{d}}_{i+1})$ by solving,

$$\mathbf{M}_{\text{eff}}\ddot{\mathbf{d}}_{i+1} = \mathbf{R}_{\text{eff}}, \qquad (15)$$

where,

$$\begin{aligned}
\mathbf{M}_{\text{eff}} &= \mathbf{M} + \mathbf{C}\gamma(\Delta t) + \mathbf{K}(\Delta t)^2\beta\\
&= \mathbf{M} + b_4\mathbf{C} + b_2\mathbf{K}, \qquad (16)\\
\mathbf{R}_{\text{eff}} &= \mathbf{F}_{i+1} - \mathbf{K}\mathbf{d}_i - [\mathbf{C} + (\Delta t)\mathbf{K}]\,\dot{\mathbf{d}}_i\\
&\quad - \Big[(1-\gamma)(\Delta t)\mathbf{C} + (0.5-\beta)(\Delta t)^2\mathbf{K}\Big]\,\ddot{\mathbf{d}}_i\\
&= \mathbf{F}_{i+1} - \mathbf{L}_0\mathbf{d}_i - \mathbf{L}_1\dot{\mathbf{d}}_i - \mathbf{L}_2\ddot{\mathbf{d}}_i. \qquad (17)
\end{aligned}$$

We, then, calculate the displacement and velocity at the $(i+1)$-th timestep using,

$$\begin{aligned}
\mathbf{d}_{i+1} &= \mathbf{d}_i + (\Delta t)\dot{\mathbf{d}}_i + (0.5-\beta)(\Delta t)^2\ddot{\mathbf{d}}_i + \beta(\Delta t)^2\ddot{\mathbf{d}}_{i+1}\\
&= \mathbf{d}_i + b_0\dot{\mathbf{d}}_i + b_1\ddot{\mathbf{d}}_i + b_2\ddot{\mathbf{d}}_{i+1}, \qquad (18)\\
\dot{\mathbf{d}}_{i+1} &= \dot{\mathbf{d}}_i + (1-\gamma)(\Delta t)\ddot{\mathbf{d}}_i + \gamma(\Delta t)\ddot{\mathbf{d}}_{i+1}\\
&= \dot{\mathbf{d}}_i + b_3\ddot{\mathbf{d}}_i + b_4\ddot{\mathbf{d}}_{i+1}. \qquad (19)
\end{aligned}$$

Solution of the forward problem can be obtained by starting with $i = 0$ and marching in time $(i \leftarrow i+1)$, using Eqs. 14–19. In Eqs. 15 to 19, we have introduced constants $b_0 - b_4$ and matrices $\mathbf{L}_0 - \mathbf{L}_2$. Their definitions are given below:

$$b_0 = \Delta t,\ \ b_1 = (\tfrac{1}{2} - \beta)(\Delta t)^2,\ \ b_2 = \beta(\Delta t)^2, \qquad (20a)$$

$$b_3 = (1-\gamma)(\Delta t),\ \ b_4 = \gamma(\Delta t), \qquad (20b)$$

$$\mathbf{L}_0 = \mathbf{K},\ \mathbf{L}_1 = \mathbf{C} + b_0\mathbf{K},\ \mathbf{L}_2 = b_3\mathbf{C} + b_1\mathbf{K}. \qquad (20c)$$

3 Load modeling

In the inverse source formulation, the surface loads are treated as unknowns. The load descriptors are updated iteratively during the inversion process (e.g., $\boldsymbol{\xi}$ in Fig. 1).

This calls for parameterization of the spatio-temporal characteristics of the loads. Specifically, the tractions $\mathbf{f}(\mathbf{x}, t)$ applied on Γ_{load} consist of contributions $\mathbf{f}_i(\mathbf{x}, t)$ from n_s sources. The i-th source consists of a spatial $\theta_i(\mathbf{x})$ and a temporal $f_i(t)$ component. θ_i is further decomposed into the x_1-directional component $\theta_{i1}(\mathbf{x})$ and the x_2-directional component $\theta_{i2}(\mathbf{x})$. Thus,

$$\mathbf{f}(\mathbf{x}, t) = \sum_{i=1}^{n_s} \mathbf{f}_i(\mathbf{x}, t) = \sum_{i=1}^{n_s} \begin{bmatrix} \theta_{i1}(\mathbf{x}) \\ \theta_{i2}(\mathbf{x}) \end{bmatrix} f_i(t). \tag{21}$$

In our numerical experiments, we use loads in either the x_1 or x_2 direction, and, thus, consistently with equipment limitations that allow load application in one direction only, either $\theta_{i1}(\mathbf{x}) = 0$ or $\theta_{i2}(\mathbf{x}) = 0$. We parameterize the (unknown) time signal using piecewise quadratic Lagrange polynomials $\tau_j(t)$ whose temporal nodal values are denoted by ξ_{ij}. This allows us to express $f_i(t)$ as

$$f_i(t) = \sum_{j=1}^{n_f} \xi_{ij} \tau_j(t), \tag{22}$$

where n_f is the total number of Lagrange polynomials. The spatial variation of the i-th load on Γ_{load} is captured by θ_{iK}, where subscript K describes the direction in which the load acts. For example, a constant pressure load applied vertically on part of the surface ($x_2 = 0$) can be expressed as

$$\theta_{i2}(x_1, 0) = H\left(\eta_i - \tfrac{b_i}{2}\right) - H\left(\eta_i + \tfrac{b_i}{2}\right), \tag{23}$$

where H is the Heaviside function, η_i is the x_1 co-ordinate of the load's center-line, and b_i is the i-th load width. A vertical load varying like a Gaussian function in space about η_i is given by

$$\theta_{i2}(x_1, 0) = -\exp\left[\tfrac{-(x_1-\eta_i)^2}{b_i}\right]. \tag{24}$$

In our numerical experiments, we use (approximately) 2-m -wide loads. Thus, we set $b_i = 2$ m in Eq. 23 and $b_i = 1.25$ m in Eq. 24.

4 The inverse source problem

Next, we discuss the formulation and solution of the inverse problem. The inverse source problem aims at maximizing a motion metric (e.g., the kinetic energy) in the target domain by seeking optimal time signals and locations for the surface tractions. In this section, we discuss the formulations for both the OTD and DTO approaches.

4.1 Optimize-then-discretize (OTD) approach

We use a standard PDE-constrained-optimization approach to resolve the inverse source problem. The objective functional is cast in its continuous form. The constraints imposed by the governing PDEs and Neumann-type boundary conditions are incorporated by augmenting the objective functional with the PDEs and boundary conditions, multiplied by *continuous* Lagrange variables. Upon discretization of the first-order optimality conditions, the resulting KKT (Karush–Kuhn–Tucker) system is solved numerically using a reduced-space approach. Maximization of the kinetic energy within the elastic inclusion (Ω_{a}) is tantamount to minimization of the following objective functional:

$$\mathcal{L} = \frac{1}{\int_{\Omega_{\text{a}}} \int_0^T \rho_{\text{a}} \left[\dot{\mathbf{u}}_{\text{a}} \cdot \dot{\mathbf{u}}_{\text{a}}\right] dt \; d\Omega}, \tag{25}$$

subject to the governing Eqs. 1 and 2, boundary, interface, and initial conditions (4)–(6). We side impose the PDEs (1) to (2c), and the boundary conditions (4b), (4d) on $\mathcal{L}$ to form the Lagrangian $\mathcal{A}$. Other boundary, initial, and interface conditions will be explicitly imposed. There results:

$$\begin{aligned}
\mathcal{A} = \; & \frac{1}{\int_{\Omega_{\text{a}}} \int_0^T \rho_{\text{a}} \left[\dot{\mathbf{u}}_{\text{a}} \cdot \dot{\mathbf{u}}_{\text{a}}\right] dt \; d\Omega} \\
& + \int_{\Omega_{\text{a}}} \int_0^T \boldsymbol{\lambda}_{u_{\text{a}}} \cdot \Big[\mu_{\text{a}} \, \mathbf{div}\left(\nabla \mathbf{u}_{\text{a}} + \nabla \mathbf{u}_{\text{a}}^T\right) \\
& \qquad + \mathbf{div}\left[\{\lambda_{\text{a}} \, \text{div} \, \mathbf{u}_{\text{a}}\} \, \mathbf{I}\right] - \rho_{\text{a}} \ddot{\mathbf{u}}_{\text{a}} \Big] \, dt \; d\Omega \\
& + \int_{\Omega_{\text{reg}}} \int_0^T \boldsymbol{\lambda}_{u_{\text{b1}}} \cdot \Big[\mu_{\text{b}} \, \mathbf{div}\left(\nabla \mathbf{u}_{\text{b}} + \nabla \mathbf{u}_{\text{b}}^T\right) \\
& \qquad + \mathbf{div}\left[\{\lambda_{\text{b}} \, \text{div} \, \mathbf{u}_{\text{b}}\} \, \mathbf{I}\right] - \rho_{\text{b}} \ddot{\mathbf{u}}_{\text{b}} \Big] \\
& + \int_{\Omega_{\text{PML}}} \int_0^T \boldsymbol{\lambda}_{u_{\text{b2}}} \cdot \Big[\mathbf{div}\left(\dot{\mathbf{S}}^T \tilde{\Lambda}_e + \mathbf{S}^T \tilde{\Lambda}_p\right) \\
& \qquad - \rho_{\text{b}} \left(\mathsf{a} \ddot{\mathbf{u}}_{\text{b}} + \mathsf{b} \dot{\mathbf{u}}_{\text{b}} + \mathsf{c} \mathbf{u}_{\text{b}}\right) \Big] \, dt \; d\Omega \\
& + \int_{\Omega_{\text{PML}}} \int_0^T \boldsymbol{\lambda}_{\text{S}} : \Big\{ \mathcal{D} : \left(\mathsf{a} \ddot{\mathbf{S}} + \mathsf{b} \dot{\mathbf{S}} + \mathsf{c} \mathbf{S}\right) \\
& \qquad - \frac{1}{2} \Big[\nabla \mathbf{u}_{\text{b}} \tilde{\Lambda}_p + \tilde{\Lambda}_p (\nabla \mathbf{u}_{\text{b}})^T \\
& \qquad + \nabla \dot{\mathbf{u}}_{\text{b}} \tilde{\Lambda}_e + \tilde{\Lambda}_e (\nabla \dot{\mathbf{u}}_{\text{b}})^T \Big] \Big\} \, dt \; d\Omega \\
& + \int_{\Gamma_{\text{load}}} \int_0^T \boldsymbol{\lambda}_{\text{F}} \cdot \Big[\Big[\mu_{\text{b}} \left(\nabla \mathbf{u}_{\text{b}} + \nabla \mathbf{u}_{\text{b}}^T\right) \\
& \qquad + \{\lambda_{\text{b}} \, \text{div} \, \mathbf{u}_{\text{b}}\} \, \mathbf{I} \Big] \mathbf{n} - \mathbf{f}(\mathbf{x}, t) \Big] \, dt \; d\Gamma \\
& + \int_{\Gamma_{\text{free}}^{\text{PML}}} \int_0^T \boldsymbol{\lambda}_{\text{b}} \cdot \left(\dot{\mathbf{S}}^T \tilde{\Lambda}_e + \mathbf{S}^T \tilde{\Lambda}_p\right) \mathbf{n} \, dt \; d\Gamma
\end{aligned} \tag{26}$$

Notice that $\boldsymbol{\lambda} = \{\boldsymbol{\lambda}_{u_{\text{a}}}, \boldsymbol{\lambda}_{u_{\text{b}}}, \boldsymbol{\lambda}_{\text{S}}, \boldsymbol{\lambda}_{\text{F}}, \boldsymbol{\lambda}_{\text{b}}\}$ are the continuous Lagrange multipliers. We, now, seek to satisfy the first-order optimality conditions.

4.1.1 State problem

The variation of the Lagrangian with respect to the Lagrange variables results in:

$$\begin{aligned}
&\delta_{\boldsymbol{\lambda}_{u_{a_i}}}\mathcal{A}=0, && i=1,2\\
&\delta_{\boldsymbol{\lambda}_{u_{b_i}}}\mathcal{A}=0, && i=1,2\\
&\delta_{\boldsymbol{\lambda}_{S_{ij}}}\mathcal{A}=0, && ij=11,12,21,22\\
&\delta_{\boldsymbol{\lambda}_{F_i}}\mathcal{A}=0, && i=1,2\\
&\delta_{\boldsymbol{\lambda}_{b_i}}\mathcal{A}=0, && i=1,2.
\end{aligned} \tag{27}$$

Equations 27 are satisfied when the (continuous) *forward problem*, i.e., Eqs. 1–6, is satisfied. The discrete form of the forward problem has been addressed in Section 2.

4.1.2 Adjoint problem - strong form

Variation of $\mathcal{A}$ with respect to the state variables yields:

$$\begin{aligned}
&\delta_{\mathbf{u}_{a_i}}\mathcal{A}=0, && i=1,2\\
&\delta_{\mathbf{u}_{b_i}}\mathcal{A}=0, && i=1,2\\
&\delta_{\mathbf{S}_{ij}}\mathcal{A}=0, && ij=11,12,21,22.
\end{aligned} \tag{28}$$

Equations 28 give rise to the strong form of the adjoint problem, for time $t\in(T,0]=\lrcorner_a$,

$$\begin{aligned}
&\mathbf{div}\left[\mu_{\mathrm{a}}\left(\nabla\boldsymbol{\lambda}_{u_{\mathrm{a}}}+\nabla\boldsymbol{\lambda}_{u_{\mathrm{a}}}^{T}\right)\right]+\mathbf{div}\left[\left\{\lambda_{\mathrm{a}}\ \mathrm{div}\ \boldsymbol{\lambda}_{u_{\mathrm{a}}}\right\}\mathbf{I}\right]\\
&\qquad -\rho_{\mathrm{a}}\ddot{\boldsymbol{\lambda}}_{u_{\mathrm{a}}}=\boldsymbol{f}_{u_a},\ \mathbf{x}\in\Omega_{\mathrm{a}},
\end{aligned} \tag{29}$$

and

$$\begin{aligned}
&\mathbf{div}\left[\mu_{\mathrm{b}}\left(\nabla\boldsymbol{\lambda}_{u_{\mathrm{b}}}+\nabla\boldsymbol{\lambda}_{u_{\mathrm{b}}}^{T}\right)\right]+\mathbf{div}\left[\left\{\lambda_{\mathrm{b}}\ \mathrm{div}\ \boldsymbol{\lambda}_{u_{\mathrm{b}}}\right\}\mathbf{I}\right]\\
&-\rho_{\mathrm{b}}\ddot{\boldsymbol{\lambda}}_{u_{\mathrm{b}}}=\mathbf{0},\quad \mathbf{x}\in\Omega_{\mathrm{reg}},
\end{aligned} \tag{30a}$$

$$\begin{aligned}
&\mathbf{div}\left(-\dot{\boldsymbol{\lambda}}_{\mathrm{S}}\tilde{\Lambda}_e+\boldsymbol{\lambda}_{\mathrm{S}}\tilde{\Lambda}_p\right)-\rho_{\mathrm{b}}\left(\mathsf{a}\ddot{\boldsymbol{\lambda}}_{u_{\mathrm{b}}}-\mathsf{b}\dot{\boldsymbol{\lambda}}_{u_{\mathrm{b}}}+\mathsf{c}\boldsymbol{\lambda}_{u_{\mathrm{b}}}\right)=\mathbf{0},\\
&\mathbf{x}\in\Omega_{\mathrm{PML}},
\end{aligned} \tag{30b}$$

$$\begin{aligned}
&\mathcal{D}:\left(\mathsf{a}\ddot{\boldsymbol{\lambda}}_{\mathrm{S}}-\mathsf{b}\dot{\boldsymbol{\lambda}}_{\mathrm{S}}+\mathsf{c}\boldsymbol{\lambda}_{\mathrm{S}}\right)+\tilde{\Lambda}_e(\nabla\dot{\boldsymbol{\lambda}}_{\mathrm{b}})^{\mathrm{T}}-\tilde{\Lambda}_p(\nabla\boldsymbol{\lambda}_{\mathrm{b}})^{\mathrm{T}}=\mathbf{0},\\
&\mathbf{x}\in\Omega_{\mathrm{PML}},
\end{aligned} \tag{30c}$$

where

$$\boldsymbol{f}_{u_a}=\mathcal{E}\rho_{\mathrm{a}}\ddot{\mathbf{u}}_{\mathrm{a}},\qquad \mathcal{E}=\frac{-2}{\left(\int_{\Omega_a}\int_0^T\rho_{\mathrm{a}}\left[\dot{\mathbf{u}}_{\mathrm{a}}\cdot\dot{\mathbf{u}}_{\mathrm{a}}\right]dt\ d\Omega\right)^2},$$

$$\boldsymbol{\lambda}_{\mathrm{S}}=\boldsymbol{\lambda}_{\mathrm{S}}^{\mathrm{sym}},$$

subject to the following boundary conditions:

$$\boldsymbol{\lambda}_{u_{\mathrm{b}}}(\mathbf{x},t)=\mathbf{0},\ \mathbf{x}\in\Gamma_{\mathrm{fixed}}^{\mathrm{PML}}, \tag{31a}$$

$$\left[\mu_{\mathrm{b}}\left(\nabla\boldsymbol{\lambda}_{u_{\mathrm{b}}}+\nabla\boldsymbol{\lambda}_{u_{\mathrm{b}}}^{T}\right)+\lambda_{\mathrm{b}}(\mathrm{div}\ \boldsymbol{\lambda}_{u_{\mathrm{b}}})\mathbf{I}\right]\mathbf{n}=\mathbf{0},\ \mathbf{x}\in\Gamma_{\mathrm{load}}, \tag{31b}$$

$$\left[\mu_{\mathrm{b}}\left(\nabla\boldsymbol{\lambda}_{u_{\mathrm{b}}}+\nabla\boldsymbol{\lambda}_{u_{\mathrm{b}}}^{T}\right)+\lambda_{\mathrm{b}}(\mathrm{div}\ \boldsymbol{\lambda}_{u_{\mathrm{b}}})\mathbf{I}\right]\mathbf{n}=\mathbf{0},\ \mathbf{x}\in\Gamma_{\mathrm{free}}, \tag{31c}$$

$$\left(-\dot{\boldsymbol{\lambda}}_{\mathrm{S}}\tilde{\Lambda}_e+\boldsymbol{\lambda}_{\mathrm{S}}\tilde{\Lambda}_p\right)\mathbf{n}=\mathbf{0},\ \mathbf{x}\in\Gamma_{\mathrm{free}}^{\mathrm{PML}}, \tag{31d}$$

$$\left(-\dot{\boldsymbol{\lambda}}_{\mathrm{S}}\tilde{\Lambda}_e+\boldsymbol{\lambda}_{\mathrm{S}}\tilde{\Lambda}_p\right)\mathbf{n}=\mathbf{0},\ \mathbf{x}\in\Gamma_{\mathrm{fixed}}^{\mathrm{PML}}, \tag{31e}$$

$$\boldsymbol{\lambda}_{\mathrm{F}}(\mathbf{x},t)=-\boldsymbol{\lambda}_{u_{\mathrm{b}}}(\mathbf{x},t),\ \mathbf{x}\in\Gamma_{\mathrm{load}}, \tag{31f}$$

$$\boldsymbol{\lambda}_{\mathrm{b}}(\mathbf{x},t)=-\boldsymbol{\lambda}_{u_{\mathrm{b}}}(\mathbf{x},t),\ \mathbf{x}\in\Gamma_{\mathrm{free}}^{\mathrm{PML}}; \tag{31g}$$

interface conditions :

$$\boldsymbol{\lambda}_{u_{\mathrm{b}}}^{+}=\boldsymbol{\lambda}_{u_{\mathrm{b}}}^{-},\ \mathbf{x}\in\Gamma_{\mathrm{I}}, \tag{32a}$$

$$\begin{aligned}
&\left(\mu_{\mathrm{b}}\left(\nabla\boldsymbol{\lambda}_{u_{\mathrm{b}}}+\nabla\boldsymbol{\lambda}_{u_{\mathrm{b}}}^{T}\right)+\lambda_{\mathrm{b}}(\mathrm{div}\ \boldsymbol{\lambda}_{u_{\mathrm{b}}})\mathbf{I}\right)\mathbf{n}_{\mathrm{I}}^{+}=\\
&\qquad -\left(-\dot{\boldsymbol{\lambda}}_{\mathrm{S}}\tilde{\Lambda}_e+\boldsymbol{\lambda}_{\mathrm{S}}\tilde{\Lambda}_p\right)\mathbf{n}_{\mathrm{I}}^{-},\ \mathbf{x}\in\Gamma_{\mathrm{I}},
\end{aligned} \tag{32b}$$

$$\boldsymbol{\lambda}_{u_{\mathrm{a}}}(\mathbf{x},t)=\boldsymbol{\lambda}_{u_{\mathrm{b}}}(\mathbf{x},t),\ \mathbf{x}\in\Gamma_{\mathrm{a}}, \tag{32c}$$

$$\boldsymbol{\lambda}_{\sigma_{\mathrm{a}}}(\mathbf{x},t)^{T}\mathbf{n}_{\mathrm{a}}^{-}=-\boldsymbol{\lambda}_{\sigma_{\mathrm{b}}}(\mathbf{x},t)^{T}\mathbf{n}_{\mathrm{a}}^{+},\ \mathbf{x}\in\Gamma_{\mathrm{a}}; \tag{32d}$$

where,

$$\boldsymbol{\lambda}_{\sigma_{\mathrm{a}}}(\mathbf{x},t)=\mu_{\mathrm{a}}\left(\nabla\boldsymbol{\lambda}_{u_{\mathrm{a}}}+\nabla\boldsymbol{\lambda}_{u_{\mathrm{a}}}^{T}\right)+\lambda_{\mathrm{a}}(\mathrm{div}\ \boldsymbol{\lambda}_{u_{\mathrm{a}}})\mathbf{I}, \tag{32e}$$

$$\boldsymbol{\lambda}_{\sigma_{\mathrm{b}}}(\mathbf{x},t)=\mu_{\mathrm{b}}\left(\nabla\boldsymbol{\lambda}_{u_{\mathrm{b}}}+\nabla\boldsymbol{\lambda}_{u_{\mathrm{b}}}^{T}\right)+\lambda_{\mathrm{b}}(\mathrm{div}\ \boldsymbol{\lambda}_{u_{\mathrm{b}}})\mathbf{I}; \tag{32f}$$

and *final* value conditions :

$$\boldsymbol{\lambda}_{u_{\mathrm{a}}}(\mathbf{x},T)=\mathbf{0},\ \dot{\boldsymbol{\lambda}}_{u_{\mathrm{a}}}(\mathbf{x},T)=-\mathcal{E}\dot{\mathbf{u}}_{\mathrm{a}},\ \mathbf{x}\in\Omega_{\mathrm{a}}, \tag{33a}$$

$$\boldsymbol{\lambda}_{u_{\mathrm{b}}}(\mathbf{x},T)=\mathbf{0},\ \dot{\boldsymbol{\lambda}}_{u_{\mathrm{b}}}(\mathbf{x},T)=\mathbf{0},\ \mathbf{x}\in\Omega_{\mathrm{reg}}, \tag{33b}$$

$$\boldsymbol{\lambda}_{S}(\mathbf{x},T)=\mathbf{0},\ \dot{\boldsymbol{\lambda}}_{S}(\mathbf{x},T)=\mathbf{0},\mathbf{x}\in\Omega_{\mathrm{PML}}. \tag{33c}$$

As it can be seen from the above, the adjoint problem is driven by the body forces that, in turn, depend on the value of the energy metric the forward problem computes over the target formation, while the time line is reversed.

4.1.3 Adjoint problem - weak form

We take an inner product of adjoint equations with appropriate test functions and integrate over the corresponding domains to obtain the following weak form of the adjoint problem:

$$\begin{aligned}
&\int_{\Omega_{\mathrm{a}}}\Big\{\nabla\mathbf{v}_{\mathrm{a}}:\left[\mu_{\mathrm{a}}\left(\nabla\boldsymbol{\lambda}_{u_{\mathrm{a}}}+\nabla\boldsymbol{\lambda}_{u_{\mathrm{a}}}^{T}\right)+\left\{\lambda_{\mathrm{a}}\ \mathrm{div}\ \boldsymbol{\lambda}_{u_{\mathrm{a}}}\right\}\mathbf{I}\right]\\
&\qquad +\mathbf{v}_{\mathrm{a}}\cdot\left[\rho_{\mathrm{a}}\ddot{\boldsymbol{\lambda}}_{u_{\mathrm{a}}}+\rho_f\ddot{\boldsymbol{\lambda}}_{w}\right]\Big\}\ d\Omega\\
&+\int_{\Omega_{\mathrm{reg}}}\Big\{\nabla\mathbf{v}_{\mathrm{b}}:\left[\mu_{\mathrm{b}}\left(\nabla\boldsymbol{\lambda}_{u_{\mathrm{b}}}+\nabla\boldsymbol{\lambda}_{u_{\mathrm{b}}}^{T}\right)+\left\{\lambda_{\mathrm{b}}\ \mathrm{div}\ \boldsymbol{\lambda}_{u_{\mathrm{b}}}\right\}\mathbf{I}\right]\\
&\qquad +\mathbf{v}_{\mathrm{b}}\cdot\rho_{\mathrm{b}}\ddot{\boldsymbol{\lambda}}_{u_{\mathrm{b}}}\Big\}\ d\Omega\\
&+\int_{\Omega_{\mathrm{PML}}}\Big\{\nabla\mathbf{v}_{\mathrm{b}}:\left(-\dot{\boldsymbol{\lambda}}_{\mathrm{S}}\tilde{\Lambda}_e+\boldsymbol{\lambda}_{\mathrm{S}}\tilde{\Lambda}_p\right)+\mathbf{v}_{\mathrm{b}}\cdot\rho_{\mathrm{b}}\left(\mathsf{a}\ddot{\boldsymbol{\lambda}}_{u_{\mathrm{b}}}\right.\\
&\qquad \left.-\mathsf{b}\dot{\boldsymbol{\lambda}}_{u_{\mathrm{b}}}+\mathsf{c}\boldsymbol{\lambda}_{u_{\mathrm{b}}}\right)d\Omega=-\int_{\Omega_{\mathrm{a}}}\mathbf{v}_{\mathrm{a}}\cdot\boldsymbol{f}_{u_a}\Big\}\ d\Omega.
\end{aligned} \tag{34a}$$

$$\begin{aligned}
&\int_{\Omega_{\mathrm{PML}}}\mathbf{T}:\Big\{\mathcal{D}:\left(\mathsf{a}\ddot{\boldsymbol{\lambda}}_{\mathrm{S}}-\mathsf{b}\dot{\boldsymbol{\lambda}}_{\mathrm{S}}+\mathsf{c}\boldsymbol{\lambda}_{\mathrm{S}}\right)+\tilde{\Lambda}_e(\nabla\dot{\boldsymbol{\lambda}}_{\mathrm{b}})^{\mathrm{T}}\\
&\qquad -\tilde{\Lambda}_p(\nabla\boldsymbol{\lambda}_{\mathrm{b}})^{\mathrm{T}}\Big\}\ d\Omega=0.
\end{aligned} \tag{34b}$$

4.1.4 Adjoint problem - semi-discrete form

We introduce spatial approximations via shape functions $\Phi(\mathbf{x})\in\mathbf{H}_h^1(\Omega)$ and $\Psi(\mathbf{x})\in\mathcal{L}_h^2(\Omega_{\mathrm{PML}})$. Thus, the trial and

test functions are given by

$$\mathbf{v}_{\mathrm{a}} = \begin{bmatrix} \mathbf{v}_{\mathrm{a}_1}^T \Phi(\mathbf{x}) \\ \mathbf{v}_{\mathrm{a}_2}^T \Phi(\mathbf{x}) \end{bmatrix}, \qquad \boldsymbol{\lambda}_{u_{\mathrm{a}}} = \begin{bmatrix} \Phi(\mathbf{x})^T \widetilde{\boldsymbol{\lambda}}_{u_{\mathrm{a}1}}(t) \\ \Phi(\mathbf{x})^T \widetilde{\boldsymbol{\lambda}}_{u_{\mathrm{a}2}}(t) \end{bmatrix},$$
$$\mathbf{v}_{\mathrm{b}} = \begin{bmatrix} \mathbf{v}_{\mathrm{b}_1}^T \Phi(\mathbf{x}) \\ \mathbf{v}_{\mathrm{b}_2}^T \Phi(\mathbf{x}) \end{bmatrix}, \qquad \boldsymbol{\lambda}_{u_{\mathrm{b}}} = \begin{bmatrix} \Phi(\mathbf{x})^T \widetilde{\boldsymbol{\lambda}}_{u_{\mathrm{b}1}}(t) \\ \Phi(\mathbf{x})^T \widetilde{\boldsymbol{\lambda}}_{u_{\mathrm{b}2}}(t) \end{bmatrix}, \tag{35a}$$

$$\mathbf{T} = \begin{bmatrix} \mathbf{T}_{11}^T \Psi(\mathbf{x}) & \mathbf{T}_{12}^T \Psi(\mathbf{x}) \\ \mathbf{T}_{21}^T \Psi(\mathbf{x}) & \mathbf{T}_{22}^T \Psi(\mathbf{x}) \end{bmatrix},$$
$$\boldsymbol{\lambda}_S = \begin{bmatrix} \Psi(\mathbf{x})^T \widetilde{\boldsymbol{\lambda}}_{S_{11}}(t) & \Psi(\mathbf{x})^T \widetilde{\boldsymbol{\lambda}}_{S_{12}}(t) \\ \Psi(\mathbf{x})^T \widetilde{\boldsymbol{\lambda}}_{S_{21}}(t) & \Psi(\mathbf{x})^T \widetilde{\boldsymbol{\lambda}}_{S_{22}}(t) \end{bmatrix}. \tag{35b}$$

We define

$$\boldsymbol{\lambda} = [\widetilde{\boldsymbol{\lambda}}_{u_{\mathrm{a}_1}} \widetilde{\boldsymbol{\lambda}}_{u_{\mathrm{a}_2}} \mid \widetilde{\boldsymbol{\lambda}}^{\mathrm{reg}}_{u_{b_1}} \widetilde{\boldsymbol{\lambda}}^{\mathrm{reg}}_{u_{b_2}} \mid \widetilde{\boldsymbol{\lambda}}^{\mathrm{PML}}_{u_{b_1}} \widetilde{\boldsymbol{\lambda}}^{\mathrm{PML}}_{u_{b_2}} \widetilde{\boldsymbol{\lambda}}_{S_{11}} \widetilde{\boldsymbol{\lambda}}_{S_{22}} \widetilde{\boldsymbol{\lambda}}_{S_{12}}]^T, \tag{36}$$

$$\mathbf{F}^{\mathrm{adj}} = [\mathbf{F}_{u_{\mathrm{a}_1}} \ \mathbf{F}_{u_{\mathrm{a}_2}} \mid \mathbf{0}\,\mathbf{0} \mid \mathbf{0}\,\mathbf{0}\,\mathbf{0}\,\mathbf{0}\,\mathbf{0}]^T, \tag{37}$$

$$\mathbf{F}_{u_{\mathrm{a}_i}}(t) = -\int_{\Omega_{\mathrm{a}}} \mathcal{E} \rho_{\mathrm{a}} \Phi \Phi^T \ddot{\widetilde{\mathbf{u}}}_{\mathrm{a}_i}(t)\, d\Omega. \tag{38}$$

Now, Eqs. 34a and 34b can be written in their semi-discrete form, using (35), as

$$\mathbf{M}^{\mathrm{adj}} \ddot{\boldsymbol{\lambda}} + \mathbf{C}^{\mathrm{adj}} \dot{\boldsymbol{\lambda}} + \mathbf{K}^{\mathrm{adj}} \boldsymbol{\lambda} = \mathbf{F}^{\mathrm{adj}}. \tag{39}$$

Comparison of Eqs. 8a and 8b with Eqs. 34a and 34b reveals that the system matrices for the forward and adjoint problems are related, as per:

$$\mathbf{M}^{\mathrm{adj}} = \mathbf{M}, \ \mathbf{C}^{\mathrm{adj}} = -\mathbf{C}, \ \mathbf{K}^{\mathrm{adj}} = \mathbf{K}. \tag{40}$$

4.1.5 Adjoint problem - time integration

The adjoint problem is a *final* BVP, and it requires traversing the time line backwards. To this end, we introduce the following approximations:

$$\boldsymbol{\lambda}_i = \boldsymbol{\lambda}_{i+1} - \dot{\boldsymbol{\lambda}}_{i+1} \Delta t + (\Delta t)^2 \left[\ddot{\boldsymbol{\lambda}}_i (0.5 - \beta) + \ddot{\boldsymbol{\lambda}}_{i+1} \beta\right], \tag{41}$$
$$\dot{\boldsymbol{\lambda}}_{i+1} = \dot{\boldsymbol{\lambda}}_{i+1} - \Delta t \left[\ddot{\boldsymbol{\lambda}}_i (1 - \gamma) + \ddot{\boldsymbol{\lambda}}_{i+1} \gamma\right] (\Delta t), \tag{42}$$

where the subscripts denote timestep. Equations 41 and 42 are used in the following system of equations:

$$\mathbf{M}^{\mathrm{adj}} \ddot{\boldsymbol{\lambda}}_{i+1} + \mathbf{C}^{\mathrm{adj}} \dot{\boldsymbol{\lambda}}_{i+1} + \mathbf{K}^{\mathrm{adj}} \boldsymbol{\lambda}_{i+1} = \mathbf{F}^{\mathrm{adj}}_{i+1}. \tag{43}$$

Inserting Eqs. 41 and 42 into Eq. 43, after some simplifications, yields,

$$\left[\mathbf{M}^{\mathrm{adj}} - \Delta t (1 - \gamma) \mathbf{C}^{\mathrm{adj}} + (\Delta t)^2 (0.5 - \beta) \mathbf{K}^{\mathrm{adj}}\right] \ddot{\boldsymbol{\lambda}}_i$$
$$= \mathbf{F}^{\mathrm{adj}}_i - \mathbf{C}^{\mathrm{adj}} \left[\dot{\boldsymbol{\lambda}}_{i+1} - \Delta t \gamma \ddot{\boldsymbol{\lambda}}_{i+1}\right]$$
$$- \mathbf{K}^{\mathrm{adj}} \left[\boldsymbol{\lambda}_{i+1} - \Delta t \dot{\boldsymbol{\lambda}}_{i+1} + (\Delta t)^2 \beta \ddot{\boldsymbol{\lambda}}_{i+1}\right]. \tag{44}$$

Similarly to the forward problem, we solve the adjoint problem using the step-by-step time integration procedure outlined by Eqs. 41–44.

4.1.6 Control problem(s)

Formulation of the control problem depends on the type of optimization to be performed. The inverse problem can be cast to obtain either the optimal time signal or the optimal position of the surface tractions, or both of the aforementioned load descriptors.

Time signal optimization: In this case, the goal of the inverse problem is to find the optimal set of parameters ξ_{ij}, as defined in Eq. 22. The control variable is given by:

$$\boldsymbol{\xi} = [\xi_{11} \ \xi_{12} \ \cdots \ \xi_{1 n_f} \ \cdots \ \xi_{(n_s)(n_f - 1)} \ \xi_{n_s n_f}]. \tag{45}$$

For a load applied in the x_k direction, the gradient of the Lagrangian with respect to the control parameter ξ_{mn} is given by

$$\nabla_{(\xi_{mn})} \mathcal{A} = \int_{\Gamma_{\mathrm{load}}} \theta_{mk}(\mathbf{x}) \Phi^T \left\{ \int_0^T \widetilde{\boldsymbol{\lambda}}_{u_b k}(t) \tau_n(t) dt \right\} d\Gamma. \tag{46}$$

Load-location optimization: Here, we seek the optimal load locations for maximizing the motion metric in the inclusion. The vector of control parameters, used in Eqs. 23 and 24, is given by $\boldsymbol{\eta} = \left[\eta_1 \ \eta_2 \cdots \eta_{n_s}\right]$.

$$\nabla_{(\eta_m)} \mathcal{A} = \int_{\Gamma_{\mathrm{load}}} \frac{\partial \theta_{mk}(\mathbf{x})}{\partial \eta_m} \Phi^T \left\{ \int_0^T \widetilde{\boldsymbol{\lambda}}_{u_b k}(t) \sum_{j=1}^{n_f} \xi_{mj} \tau_j(t) dt \right\} d\Gamma. \tag{47}$$

Detailed derivations of the control problems are given in Appendix B.

The summary of the inversion procedure is discussed next. We solve the forward problem using an initial guess of the source characteristics to obtain the state variables. We use the state variables to form the body forces that drive the adjoint problem. Upon solution, the adjoint problem yields the values of the adjoint variable on the loaded boundary Γ_{load}. These values are used to compute the reduced gradient(s) in Eqs. 46 and/or 47. The procedure used for updating the vector of location parameters ($\boldsymbol{\eta}$) is discussed next; the identical procedure is used for updating the vector of time parameters ($\boldsymbol{\xi}$). Let $\mathbf{g}_{lk}$ be the discretized reduced gradient for the load location vector obtained at the end of the k-th inversion iteration. Thus,

$$\mathbf{g}_{lk} = (\nabla_{(\boldsymbol{\eta})} \mathcal{A})_k. \tag{48}$$

$\mathbf{g}_{lk}$ is used to compute a *search direction* $\mathbf{s}_{lk}$ in the space

of source characteristics. Here, we use the search direction given by the conjugate gradient method.

$$\begin{aligned} \mathbf{s}_{lk} &= -\mathbf{g}_{lk}, \text{ if } k = 0, \\ \mathbf{s}_{lk} &= -\mathbf{g}_{lk} + \frac{\mathbf{g}_{lk} \cdot \mathbf{g}_{lk}}{\mathbf{g}_{l(k-1)} \cdot \mathbf{g}_{l(k-1)}}, \text{ otherwise.} \end{aligned} \tag{49}$$

We, then, update the source characteristics by taking a *step* towards the search direction. The magnitude of the step is decided by the step length α_{lk}, i.e., we set $\boldsymbol{\eta}_{k+1} = \boldsymbol{\eta}_k + \alpha_{lk}\mathbf{s}_{lk}$. The iteration counter is updated ($k \leftarrow k+1$), and the procedure is repeated until convergence is reached.

4.1.7 Discrete objective functional

To complete the discrete problem, the objective functional (25) must also be discretized. Let $\hat{\mathcal{L}}$ denote the discrete $\mathcal{L}$; then

$$\hat{\mathcal{L}} = \frac{1}{\int_0^T \tilde{\dot{\mathbf{u}}}_{\mathrm{a}}^T \mathbf{M}^{\mathrm{a}} \tilde{\dot{\mathbf{u}}}_{\mathrm{a}} dt}, \tag{50}$$

where $\mathbf{M}^{\mathrm{a}}$ is the mass matrix of the inclusion (Appendix A).

4.2 Discretize-then-optimize (DTO) approach

Following the procedure outlined in [11, 15], we begin with the spatio-temporally discretized forward problem. The objective functional is cast in a discrete form and augmented by weighing the governing equations by discrete Lagrange multipliers. The resulting *discrete* Lagrangian is then subjected to the first-order optimality conditions to arrive at the KKT system. Specifically, the time-marching scheme outlined in Eqs. 14 to 19 can be represented as a linear system of equations given by,

$$\boldsymbol{Q}\boldsymbol{u} = \boldsymbol{f}, \tag{51}$$

where

$$\boldsymbol{u} = [\ddot{\mathbf{d}}_0\ \dot{\mathbf{d}}_0\ \mathbf{d}_0\ \ddot{\mathbf{d}}_1\ \dot{\mathbf{d}}_1\ \mathbf{d}_1\ \cdots\ \ddot{\mathbf{d}}_N\ \dot{\mathbf{d}}_N\ \mathbf{d}_N\ ]^T, \tag{52}$$

$$\boldsymbol{f} = [\mathbf{F}_0\ \dot{\mathbf{d}}_0\ \mathbf{d}_0\ \mathbf{F}_1\ \mathbf{0}\ \mathbf{0}\ \cdots\ \mathbf{F}_N\ \mathbf{0}\ \mathbf{0}]^T, \tag{53}$$

$$\boldsymbol{Q} = \left[\begin{array}{cccccccccc} \mathbf{M} & \mathbf{C} & \mathbf{K} & \mathbf{0} & \mathbf{0}\,\mathbf{0}\cdots & \mathbf{0} & \mathbf{0} & \mathbf{0} & \mathbf{0} & \mathbf{0}\,\mathbf{0} \\ \mathbf{0} & \mathbf{I} & \mathbf{0} & \mathbf{0} & \mathbf{0}\,\mathbf{0}\cdots & \mathbf{0} & \mathbf{0} & \mathbf{0} & \mathbf{0} & \mathbf{0}\,\mathbf{0} \\ \mathbf{0} & \mathbf{0} & \mathbf{I} & \mathbf{0} & \mathbf{0}\,\mathbf{0}\cdots & \mathbf{0} & \mathbf{0} & \mathbf{0} & \mathbf{0} & \mathbf{0}\,\mathbf{0} \\ \hline \mathbf{L}_2 & \mathbf{L}_1 & \mathbf{L}_0 & \mathbf{M}_{\mathrm{eff}} & \mathbf{0}\,\mathbf{0}\cdots & \mathbf{0} & \mathbf{0} & \mathbf{0} & \mathbf{0} & \mathbf{0}\,\mathbf{0} \\ -b_3\mathbf{I} & -\mathbf{I} & \mathbf{0} & -b_4\mathbf{I} & \mathbf{I}\,\mathbf{0}\cdots & \mathbf{0} & \mathbf{0} & \mathbf{0} & \mathbf{0} & \mathbf{0}\,\mathbf{0} \\ -b_1\mathbf{I} & -b_0\mathbf{I} & -\mathbf{I} & -b_2\mathbf{I} & \mathbf{0}\,\mathbf{I}\cdots & \mathbf{0} & \mathbf{0} & \mathbf{0} & \mathbf{0} & \mathbf{0}\,\mathbf{0} \\ \hline \vdots & \vdots & \vdots & \vdots & \vdots\,\vdots\,\ddots & \vdots & \vdots & \vdots & \vdots & \vdots\,\vdots \\ \hline \mathbf{0} & \mathbf{0} & \mathbf{0} & \mathbf{0} & \mathbf{0}\,\mathbf{0}\cdots & \mathbf{L}_2 & \mathbf{L}_1 & \mathbf{L}_0 & \mathbf{M}_{\mathrm{eff}} & \mathbf{0}\,\mathbf{0} \\ \mathbf{0} & \mathbf{0} & \mathbf{0} & \mathbf{0} & \mathbf{0}\,\mathbf{0}\cdots & -b_3\mathbf{I} & -\mathbf{I} & \mathbf{0} & -b_4\mathbf{I} & \mathbf{I}\,\mathbf{0} \\ \mathbf{0} & \mathbf{0} & \mathbf{0} & \mathbf{0} & \mathbf{0}\,\mathbf{0}\cdots & -b_1\mathbf{I} & -b_0\mathbf{I} & -\mathbf{I} & -b_2\mathbf{I} & \mathbf{0}\,\mathbf{I} \end{array}\right]. \tag{54}$$

Equation 51, which is tantamount to the discretized forward problem, will be used to formulate the inverse problem. Recall that the objective functional was given by Eq. 25 in its continuous form. The corresponding discrete form, modulo the mass matrix for compactness, is given by (compare with (50)):

$$\begin{aligned} \mathcal{L}_d &= \frac{1}{\int_0^T \rho_{\mathrm{a}} \tilde{\dot{\mathbf{u}}}_{\mathrm{a}}^T \tilde{\dot{\mathbf{u}}}_{\mathrm{a}} dt} \\ &\simeq \frac{1}{\rho_{\mathrm{a}}\ \Delta t\ [\frac{1}{2}\tilde{\dot{\mathbf{u}}}_{\mathrm{a}_0}^T \tilde{\dot{\mathbf{u}}}_{\mathrm{a}_0} + \frac{1}{2}\tilde{\dot{\mathbf{u}}}_{\mathrm{a}_N}^T \tilde{\dot{\mathbf{u}}}_{\mathrm{a}_N} + \sum_{i=1}^{N-1} \tilde{\dot{\mathbf{u}}}_{\mathrm{a}_i}^T \tilde{\dot{\mathbf{u}}}_{\mathrm{a}_i}]} \\ &= \frac{1}{\rho_{\mathrm{a}} \boldsymbol{u}^T \boldsymbol{B}_{u_{\mathrm{a}}} \boldsymbol{u}}, \end{aligned} \tag{55}$$

where $\boldsymbol{B}_{u_{\mathrm{a}}}$ is a block diagonal matrix with $\Delta t \boldsymbol{B}_{\mathrm{i}}$ on its diagonals; $\boldsymbol{B}_{\mathrm{i}}$ are square matrices that are zero everywhere except on diagonals that correspond to the $\dot{\mathbf{u}}_{\mathrm{a}}$ degrees of freedom. As before, we superimpose the governing equations (51), weighted by the discrete Lagrange multipliers $\boldsymbol{p}$, on the objective functional to obtain the discrete Lagrangian, which is to be minimized. Thus, the constrained minimization problem can now be stated as,

$$\min_{f}\ \mathcal{A}_d(\boldsymbol{u}, \boldsymbol{p}, \boldsymbol{f}) = \mathcal{L}_d - \boldsymbol{p}^T(\boldsymbol{Q}\boldsymbol{u} - \boldsymbol{f}), \tag{56}$$

where

$$\boldsymbol{p} = [\ddot{\boldsymbol{\lambda}}_0\ \dot{\boldsymbol{\lambda}}_0\ \boldsymbol{\lambda}_0\ \ddot{\boldsymbol{\lambda}}_1\ \dot{\boldsymbol{\lambda}}_1\ \boldsymbol{\lambda}_1\ \cdots\ \ddot{\boldsymbol{\lambda}}_N\ \dot{\boldsymbol{\lambda}}_N\ \boldsymbol{\lambda}_N\ ]^T, \tag{57}$$

$$\boldsymbol{\lambda} = [\tilde{\boldsymbol{\lambda}}_{u_{\mathrm{a}_1}} \tilde{\boldsymbol{\lambda}}_{u_{\mathrm{a}_2}} \mid \tilde{\boldsymbol{\lambda}}_{u_{b_1}}^{\mathrm{reg}} \tilde{\boldsymbol{\lambda}}_{u_{b_2}}^{\mathrm{reg}} \mid \tilde{\boldsymbol{\lambda}}_{u_{b_1}}^{\mathrm{PML}} \tilde{\boldsymbol{\lambda}}_{u_{b_2}}^{\mathrm{PML}} \tilde{\boldsymbol{\lambda}}_{S_{11}} \tilde{\boldsymbol{\lambda}}_{S_{22}} \tilde{\boldsymbol{\lambda}}_{S_{12}}]^T, \tag{58}$$

$$\boldsymbol{\lambda}_i = \boldsymbol{\lambda}, \text{ at } t = i\Delta t. \tag{59}$$

The first-order optimality conditions can now be obtained by taking derivatives of $\mathcal{A}_d$ with respect to $\boldsymbol{u}, \boldsymbol{\lambda}$ and the force-parameters ξ, η.

4.2.1 State problem

$$\frac{\partial \mathcal{A}_d}{\partial \boldsymbol{p}} = \mathbf{0} \implies \boldsymbol{Q}\boldsymbol{u} = \boldsymbol{f}, \tag{60}$$

which is the *forward* problem, given by Eq. 51.

4.2.2 Adjoint problem

$$\frac{\partial \mathcal{A}_d}{\partial \boldsymbol{u}} = \mathbf{0} \implies \boldsymbol{Q}^T \boldsymbol{p} = \frac{-2\boldsymbol{B}_{u_{\mathrm{a}}}\boldsymbol{u}}{\rho_{\mathrm{a}}\ (\boldsymbol{u}^T \boldsymbol{B}_{u_{\mathrm{a}}} \boldsymbol{u})^2}. \tag{61}$$

Equation 61 represents the *adjoint* problem associated with the inverse problem of interest. Since the adjoint problem involves transpose of $\boldsymbol{Q}$, we solve it by marching backwards in time. That is, from the last three rows of the matrix (61),

we get, (for $i = N$),

$$\text{(update)}\quad \boldsymbol{\lambda}_N = \boldsymbol{\lambda}_N^{\mathrm{u}}, \tag{62a}$$

$$\text{(update)}\quad \dot{\boldsymbol{\lambda}}_N = \boldsymbol{\lambda}_N^{\mathrm{v}}, \tag{62b}$$

$$\text{(solve)}\quad \mathbf{M}_{\mathrm{eff}}^T \ddot{\boldsymbol{\lambda}}_N = \boldsymbol{\lambda}_N^{\mathrm{a}} + b_4 \dot{\boldsymbol{\lambda}}_N + b_2 \boldsymbol{\lambda}_N. \tag{62c}$$

For $(N-1) \leq i \leq 1$, we update $\dot{\boldsymbol{\lambda}}_i$, $\boldsymbol{\lambda}_i$ and solve for $\ddot{\boldsymbol{\lambda}}_i$ using the following,

$$\text{(update)}\quad \boldsymbol{\lambda}_i = \boldsymbol{\lambda}_i^{\mathrm{u}} + \boldsymbol{\lambda}_{i+1} - \mathbf{L}_0^T \ddot{\boldsymbol{\lambda}}_{i+1}, \tag{63a}$$

$$\text{(update)}\quad \dot{\boldsymbol{\lambda}}_i = \boldsymbol{\lambda}_i^{\mathrm{v}} + b_0 \boldsymbol{\lambda}_{i+1} + \dot{\boldsymbol{\lambda}}_{i+1} - \mathbf{L}_1^T \ddot{\boldsymbol{\lambda}}_{i+1}, \tag{63b}$$

$$\text{(solve)}\quad \mathbf{M}_{\mathrm{eff}}^T \ddot{\boldsymbol{\lambda}}_i = \boldsymbol{\lambda}_i^{\mathrm{a}} + b_1 \boldsymbol{\lambda}_{i+1} + b_3 \dot{\boldsymbol{\lambda}}_{i+1} - \mathbf{L}_2^T \ddot{\boldsymbol{\lambda}}_{i+1} + b_2 \boldsymbol{\lambda}_i + b_4 \dot{\boldsymbol{\lambda}}_i. \tag{63c}$$

For $i = 0$, we get

$$\text{(solve)}\mathbf{M}^T \ddot{\boldsymbol{\lambda}}_0 = \boldsymbol{\lambda}_0^{\mathrm{a}} + b_1 \boldsymbol{\lambda}_1 + b_3 \dot{\boldsymbol{\lambda}}_1 - \mathbf{L}_2^T \ddot{\boldsymbol{\lambda}}_1, \tag{64a}$$

$$\text{(update)}\boldsymbol{\lambda}_0 = \boldsymbol{\lambda}_0^{u} + \boldsymbol{\lambda}_1 - \mathbf{L}_0^T \ddot{\boldsymbol{\lambda}}_1 - \mathbf{K}^T \ddot{\boldsymbol{\lambda}}_0, \tag{64b}$$

$$\text{(update)}\dot{\boldsymbol{\lambda}}_0 = \boldsymbol{\lambda}_0^{\mathrm{v}} + b_0 \boldsymbol{\lambda}_1 + \dot{\boldsymbol{\lambda}}_1 - \mathbf{L}_1^T \ddot{\boldsymbol{\lambda}}_1 - \mathbf{C}^T \ddot{\boldsymbol{\lambda}}_0. \tag{64c}$$

In Eqs. 62–64,

$$\boldsymbol{\lambda}_{\mathrm{i}}^{\mathrm{u}} = \boldsymbol{\lambda}_{\mathrm{i}}^{\mathrm{a}} = \mathbf{0},\ 0 \leq i \leq N, \tag{65a}$$

$$\boldsymbol{\lambda}_{\mathrm{i}}^{\mathrm{v}} = -\rho_{\mathrm{a}}\, \Delta t\, \mathcal{L}_d^2 [\tilde{\ddot{\mathbf{u}}}_{a_{1\mathrm{i}}} \tilde{\ddot{\mathbf{u}}}_{a_{2\mathrm{i}}} \mid \mathbf{0\,0} \mid \mathbf{0\,0\,0\,0\,0}]^T,\ \mathrm{i} = 0, N, \tag{65b}$$

$$\boldsymbol{\lambda}_{\mathrm{i}}^{\mathrm{v}} = -2\rho_{\mathrm{a}}\, \Delta t\, \mathcal{L}_d^2 [\tilde{\ddot{\mathbf{u}}}_{a_{1\mathrm{i}}} \tilde{\ddot{\mathbf{u}}}_{a_{2\mathrm{i}}} \mid \mathbf{0\,0} \mid \mathbf{0\,0\,0\,0\,0}]^T,\ 0 < \mathrm{i} < N. \tag{65c}$$

It can be seen from the above equations that the adjoint problem of the DTO approach is driven by the prescription of velocity-like adjoint variables ($\boldsymbol{\lambda}_{\mathrm{i}}^{\mathrm{v}}$) at each time step. The value of $\boldsymbol{\lambda}_{\mathrm{i}}^{\mathrm{v}}$ depends on the value of the objective functional as well as the value of the velocity vector for the target ($\dot{\mathbf{u}}_{\mathrm{a}_i}$).

4.2.3 Control problem(s)

Time signal optimization:

$$\frac{\partial \mathcal{A}_d}{\partial \xi} = \boldsymbol{p}^T \frac{\partial \boldsymbol{f}}{\partial \xi} \tag{66}$$

provides the gradient of the Lagrangian with respect to the control parameter ξ. For any given nodal-excitation parameter ξ_{mn}, we get

$$\frac{\partial \mathcal{A}_d}{\partial \xi_{mn}} = \sum_{i=0}^{N} \ddot{\boldsymbol{\lambda}}_i^T \frac{\partial \mathbf{F}_i}{\partial \xi_{mn}}. \tag{67}$$

For a load acting in the x_p direction, we update each element, ξ_{mn}, of the control parameter vector $\boldsymbol{\xi}$ using:

$$\begin{aligned}\frac{\partial \mathcal{A}_d}{\partial \xi_{mn}} &= \sum_{k=0}^{N} \ddot{\boldsymbol{\lambda}}_{k,\mathrm{load}}^T \int_{\Gamma_{\mathrm{load}}} \theta_{mp}(\mathbf{x}) \Phi\ \tau_n(k\Delta t)\ d\Gamma, \\ &= \sum_{k=0}^{N} \tau_n(k\Delta t)\ \ddot{\boldsymbol{\lambda}}_{k,\mathrm{load}}^T \int_{\Gamma_{\mathrm{load}}} \theta_{mp}(\mathbf{x}) \Phi\ d\Gamma.\end{aligned} \tag{68}$$

Load location optimization:

$$\frac{\partial \mathcal{A}_d}{\partial \eta} = \boldsymbol{p}^T \frac{\partial \boldsymbol{f}}{\partial \eta} \tag{69}$$

provides the gradient of the Lagrangian with respect to the control parameter η. For any given load-location parameter η_m, we get

$$\frac{\partial \mathcal{A}_d}{\partial \eta_m} = \sum_{i=0}^{N} \ddot{\boldsymbol{\lambda}}_i^T \frac{\partial \mathbf{F}_i}{\partial \eta_m}. \tag{70}$$

For a load acting in the x_p direction, we update each element, η_m, of the control parameter vector $\boldsymbol{\eta}$ using:

$$\begin{aligned}\frac{\partial \mathcal{A}_d}{\partial \eta_m} &= \sum_{k=0}^{N} \ddot{\boldsymbol{\lambda}}_{k,\mathrm{load}}^T \int_{\Gamma_{\mathrm{load}}} \frac{\partial \theta_{mp}(\mathbf{x})}{\partial \eta_m} \Phi \sum_{j=1}^{n_f} \xi_{mj} \tau_j(k\Delta t)\ d\Gamma, \\ &= \sum_{k=0}^{N} \left[\left(\sum_{j=1}^{n_f} \xi_{mj} \tau_j(k\Delta t) \right) \cdot \ddot{\boldsymbol{\lambda}}_{k,\mathrm{load}}^T \int_{\Gamma_{\mathrm{load}}} \frac{\partial \theta_{mp}(\mathbf{x})}{\partial \eta_m} \Phi\ d\Gamma \right].\end{aligned} \tag{71}$$

Effectively, Eqs. 68 and 71 of the DTO approach are used in lieu of Eqs. 46 and 47 of the OTD approach. Details of the derivations are given in Appendix B.

As before, we start the inversion process with an initial guess of source characteristics. We solve the forward problem, compute the objective functional ($\mathcal{L}_d$), and obtain the velocity field in the target ($\dot{\mathbf{u}}_{\mathrm{a}_i}$). $\mathcal{L}_d$ and $\dot{\mathbf{u}}_{\mathrm{a}_i}$ are used to compute the velocity-like adjoint variables ($\boldsymbol{\lambda}_{\mathrm{i}}^{\mathrm{v}}$) that drive the adjoint problem. Solution of the adjoint problem yields the values of the acceleration-like adjoint variables on the loaded boundary ($\ddot{\boldsymbol{\lambda}}_{k,\mathrm{load}}$). We, then, use Eqs. 68 and/or 71

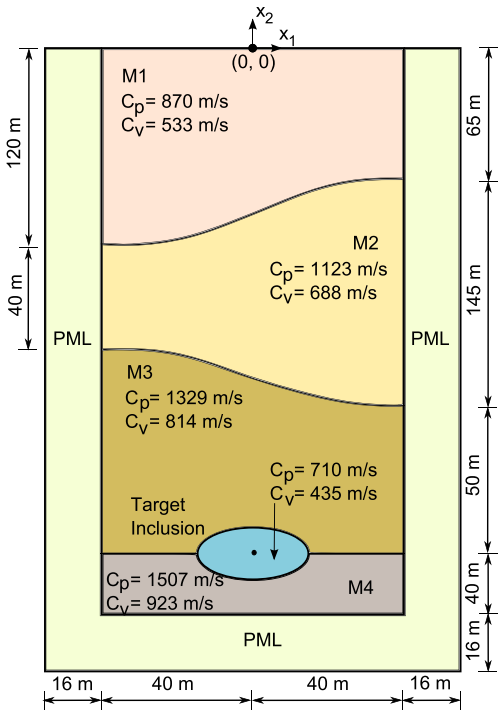

Fig. 4 Geological formation model

Table 1 Summary of numerical experiments

Numerical experiment number	Loading direction	Spatial description of loads	Optimization algorithm	Optimization variable	KE_{inc} (J/m)
1	Vertical	Eq. 23	OTD	Time-signal	1.63
2	Horizontal	Eq. 24	DTO	Time-signal	3.22
				Time-signal then load-location (sequentially)	3.85
				Time-signal and load-location (simultaneously)	4.75
3	Vertical	Eq. 23	OTD	Time-signal	1.63
3	Horizontal	Eq. 23	OTD	Time-signal	3.10
4	Horizontal	Eq. 23	OTD	Time-signal	3.09
4	Horizontal	Eq. 23	DTO	Time-signal	3.10

to compute the discrete reduced gradients. Equations 48 and 49 are then employed to update the source characteristics, and we follow the iterative inversion procedure until convergence is reached.

5 Numerical experiments

In this section, we test the inversion algorithm by conducting numerical experiments. In our experiments, we use either horizontally- or vertically-polarized surface loads. The maximum amplitude is set at 50 kN/m^2. Figure 4 shows the geometry as well as the P- and S-wave speeds for the geological formation model used to illustrate the capabilities of the methodology. The mass densities (ρ_a and ρ_b) for all materials in the profile shown in Fig. 4 are 2200 kg/m^3. The profile has an elliptical target inclusion whose center is located at 260 m below the ground surface. The major axis of the inclusion is 30 m long, while the minor axis length is 15 m. In all experiments, we use a timestep $\Delta t = 0.001$ s.

We define the following metrics to evaluate the performance of the proposed inversion method: if $\mathbf{u}(t)$ denotes the displacement at a computational node at time t, the time-averaged kinetic energy (KE_{TA}) at that node is defined as

$$KE_{TA} = \int_0^T \frac{1}{2}\rho\,[\dot{\mathbf{u}}(t)\cdot\dot{\mathbf{u}}(t)]\,dt \;/\; T, \tag{72}$$

where ρ is the mass density. Time-averaged kinetic energy, further integrated over the target inclusion, is defined as

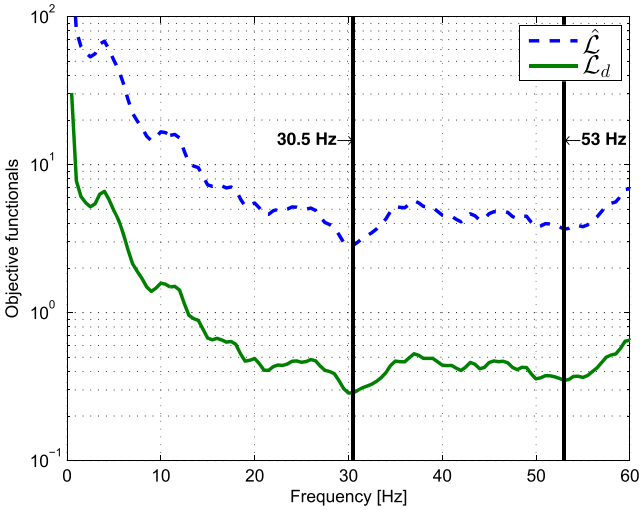

Fig. 5 Frequency sweep results for uniform vertical load

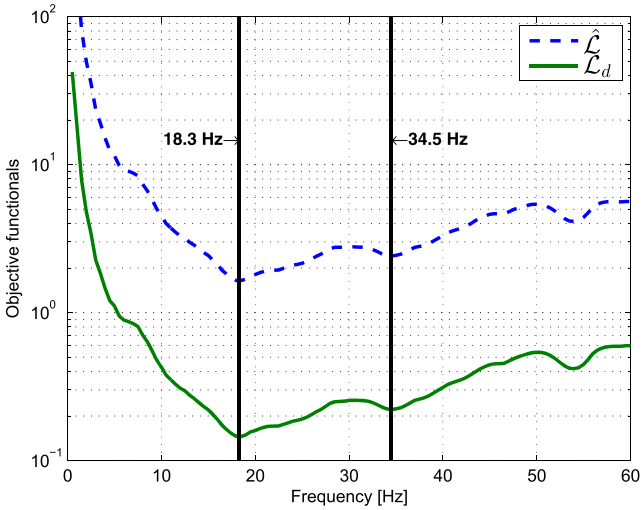

Fig. 6 Frequency sweep results for uniform horizontal load

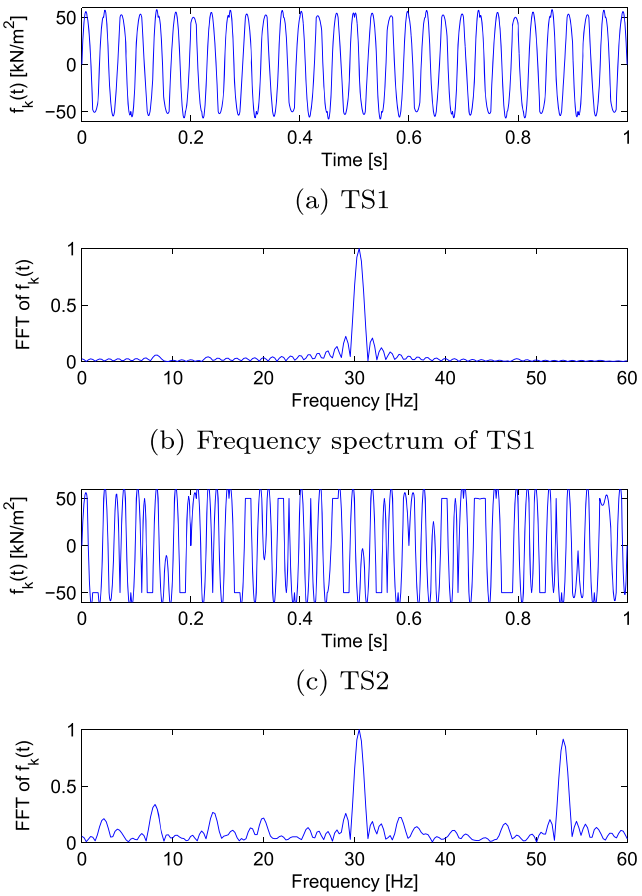

(a) TS1

(b) Frequency spectrum of TS1

(c) TS2

(d) Frequency spectrum of TS2

Fig. 7 Experiment 1—TS1 and TS2 signals

$\mathrm{KE_{inc}}$. Thus,

$$\mathrm{KE_{inc}} = \int_{\Omega_a}\int_0^T \frac{1}{2}\rho_a\,[\dot{\mathbf{u}}_a(t)\cdot\dot{\mathbf{u}}_a(t)]\,dt\;d\Omega\;/\;T$$
$$= \int_0^T \frac{1}{2}\tilde{\dot{\mathbf{u}}}_a(t)^T\mathbf{M}^a\tilde{\dot{\mathbf{u}}}_a(t)dt\;/\;T, \tag{73}$$

where $\tilde{\dot{\mathbf{u}}}_a(t)$ is the velocity vector corresponding to the computational nodes in the inclusion, and $\mathbf{M}^a$ is the mass matrix of the inclusion, as defined in Appendix A. We remark that the units of $\mathrm{KE_{TA}}$ are joule per cubic meter and those of $\mathrm{KE_{inc}}$ are joule per meter. In the experiments, we use plots of $\mathrm{KE_{TA}}$ and values of $\mathrm{KE_{inc}}$ to compare the degree of energy focusing achieved by various techniques. We report the results of four numerical experiments, which are used to highlight the performance of the inverse source approach; Table 1 shows a summary of the numerical experiments features, and the kinetic energy $\mathrm{KE_{inc}}$ density resulting from each experiment.

As discussed earlier, a frequency sweep is one possibility for deciding suitable temporal characteristics of the wave sources. In our experiments, we compare the performance of the inversion technique with that of the frequency sweep approach. To this end, we conduct a frequency sweep for the geological formation model (Fig. 4) by applying first a uniform surface load, either horizontally or vertically polarized. The load has an amplitude of 2 $\mathrm{kN/m^2}$ everywhere along the line $x_2 = 0$, and, temporally, it varies as a sine function of the driving frequency. We calculate the objective functionals ($\hat{\mathcal{L}}$ and $\mathcal{L}_d$) for frequencies ranging between 0.5 and 60 Hz.

Figure 5 shows that for the vertically-acting load, there are many local minima at various driving frequencies. The global minimum occurs at 30.5 Hz. Notice that the value of the local minimum at 53 Hz is very close to that of the global minimum. For the horizontal load (Fig. 6), the objective functionals have a global minimum at 18.3 Hz. The figure also shows that both objective functionals exhibit a second strong local minimum at a driving frequency of 34.5 Hz.

5.1 Experiment 1—Source signal optimization

In this experiment, we compare the results of the time signal optimization with those of the frequency sweep procedure. The performance is judged by comparing $\mathrm{KE_{inc}}$ for the two approaches. To this end, we apply three vertical loads centered at (10,0)m, (−15, 0)m, and (0,0)m on the surface ($x_2 = 0$) of the geological formation model. We use Eq. 23 to specify the spatial variability of the loads. If one were to choose time signals based on the results of the frequency sweep (Fig. 5), there are (at least) two possibilities: (i) monochromatic signals having 30.5 Hz as their dominant frequency and (ii) dichromatic signals having 30.5 and 53 Hz as dominant frequencies. To measure the energy delivery performance of these signals, we construct

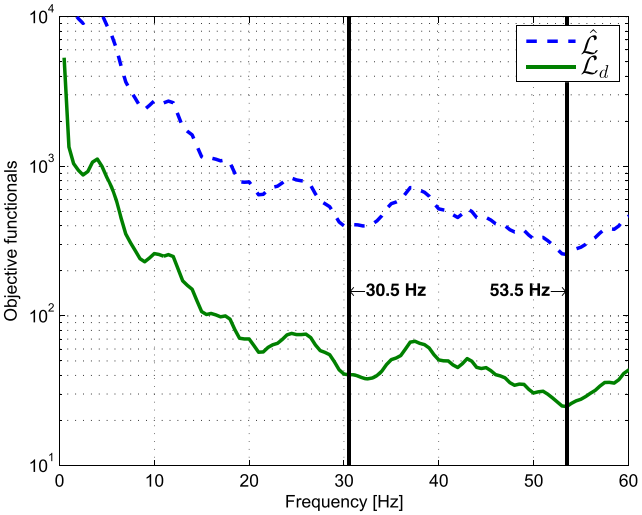

Fig. 8 Frequency sweep results for three vertical loads located at (10,0)m, (−15, 0)m, and (0,0)m

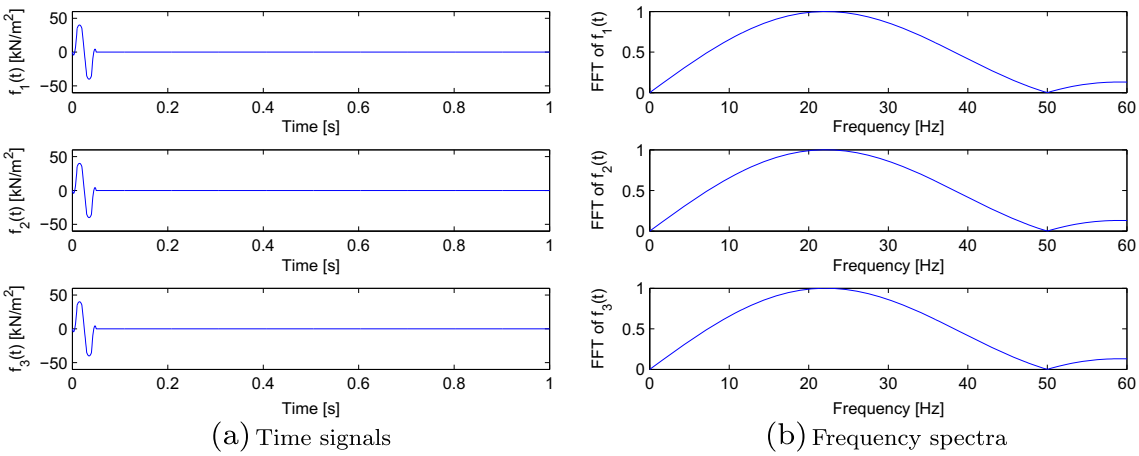

(a) Time signals (b) Frequency spectra

Fig. 9 Experiment 1–Initial guess

signals TS1 and TS2 using piecewise quadratic Lagrange polynomials (22), corresponding to the monochromatic and dichromatic signal, respectively. The time signals (TS1 and TS2) and their frequency spectra are shown in Fig. 7 measure KE_{inc} for these two cases.

Sources operating with TS1 as their driving signals are able to achieve $KE_{inc} = 1.06$ J/m, whereas those with TS2 as the driving signals deliver KE_{inc} of 1.39 J/m. In other words, operating three vertical loads at the combination of two sine functions, each operating at the two "best" frequencies obtained by the frequency sweep will result in an increase of the energy delivery of about 36 % over the energy delivered when operating the same three loads at the single best frequency resulting from the sweep. We remark that loading the entire width of the computational domain generates waves having, initially, plane wavefronts in the domain of interest. The waves emitted by the finite-width sources are near-cylindrical in nature. This difference alone will not alter in any significant way the sweep's results. For example, if three 2-m-wide vertically-acting loads operate at the same three locations as before, the same (approximately) minima would be recovered, as the plot in Fig. 8 depicts.

Of interest is how the inversion procedure will perform. Thus, next, we conduct the time signal optimization using the OTD approach (without changing the load locations). The initial guess for the time signals of the loads is shown in Fig. 9. It can be seen in Fig. 9b that the initial guesses have broad frequency support. The time signals obtained following the optimization are shown in Fig. 10, and as it can be seen in Fig. 10b for all three loads there are clearly two dominant frequencies at, approximately, 30 and 53.5 Hz. That is, the optimizer converged nicely to signals that, at a minimum, contain dominant contributions from the two "best" frequencies revealed by the frequency sweep, without any prior biasing of the inversion process. Notice also that the converged time signals have a rich content, with contributions from many frequencies other than those corresponding to the strongest minima seen in the frequency sweep. It can also be observed in Fig. 10b that the frequency spectra for

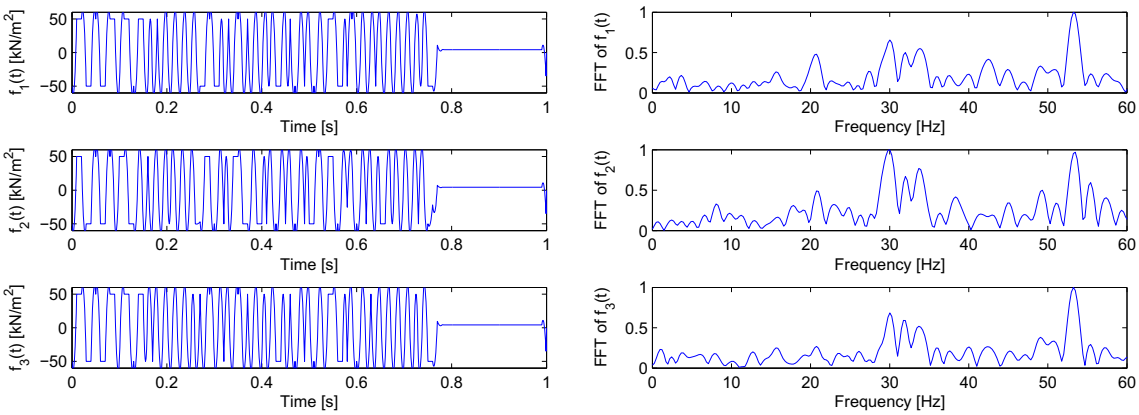

(a) Time signals (b) Frequency spectra

Fig. 10 Experiment 1— Converged time signals

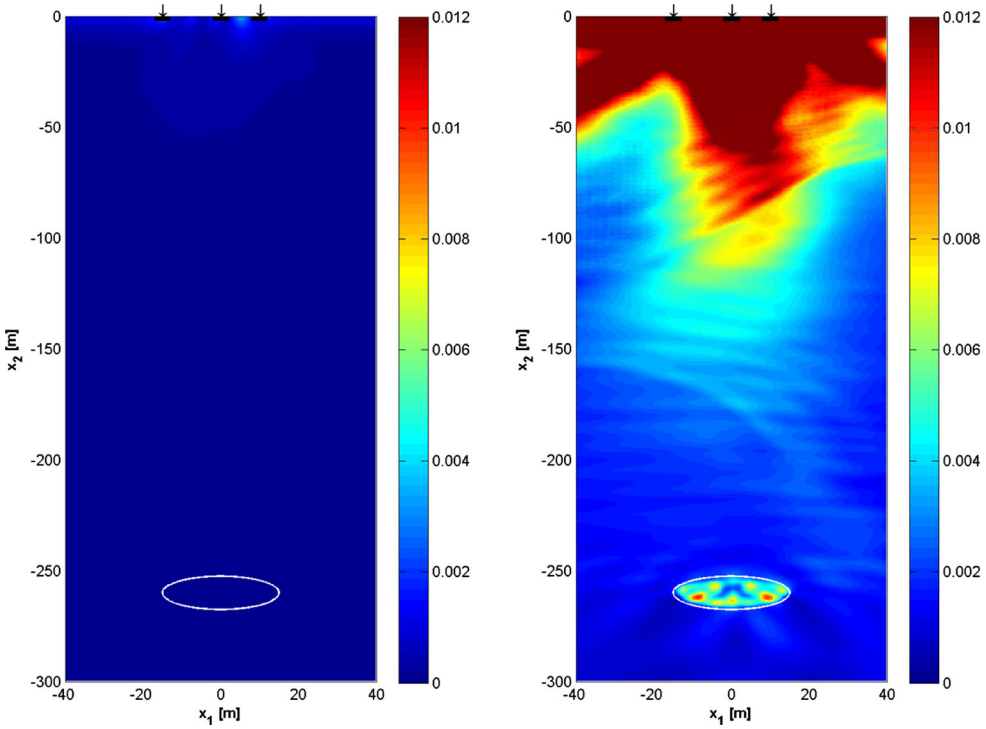

(a) KE_{TA} for the initial guess of time signals, loads located at (10,0)m, (-15,0)m, and (0,0)m

(b) KE_{TA} after time signal optimization, loads located at (10,0)m, (-15,0)m, and (0,0)m

Fig. 11 Experiment 1—Time-averaged kinetic energy

the converged signals of the three loads are not identical. The difference can be attributed to the complex interacting wave patterns. Simply put, the inverse source problem is *aware* of these patterns by virtue of the forward (state) problem solution, and *uses* the information to steer the time signals to maximize energy focusing. Figure 11 depicts the distribution of time-averaged kinetic energy (KE_{TA}) in the computational domain before and after optimization; the KE_{inc} delivered to the target due to the optimized time signals is 1.63 J/m.

This experiment highlights the key differences between the frequency sweep and time signal optimization procedures. The time signal optimization procedure was able to deliver about 17 % more kinetic energy (in the time-averaged sense) than the best the frequency sweep information could do based on the dichromatic signal. Note that we conducted our experiment for a duration T = 1 s: in a field implementation of the seismic EOR, where the stimulation may be applied for days, 17 % improvement in the efficiency is significant. For the model formation used

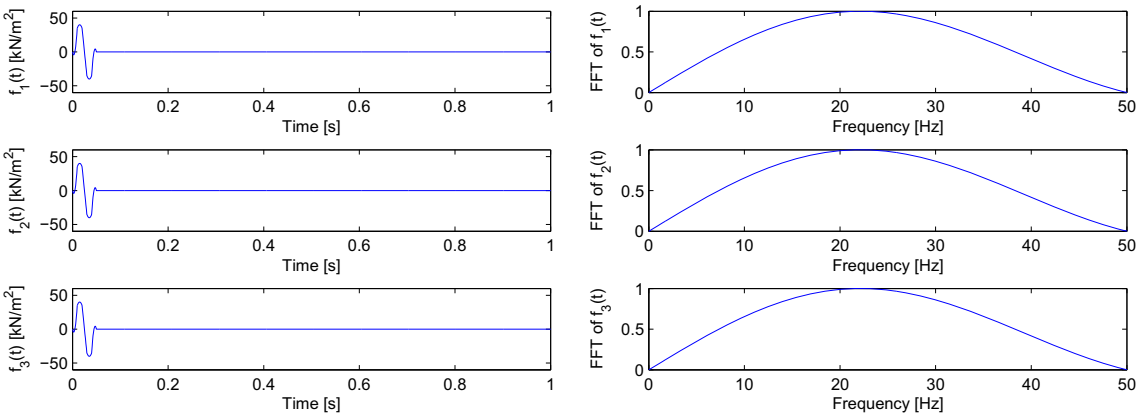

(a) Time signals

(b) Frequency spectra

Fig. 12 Experiment 2—Initial guess

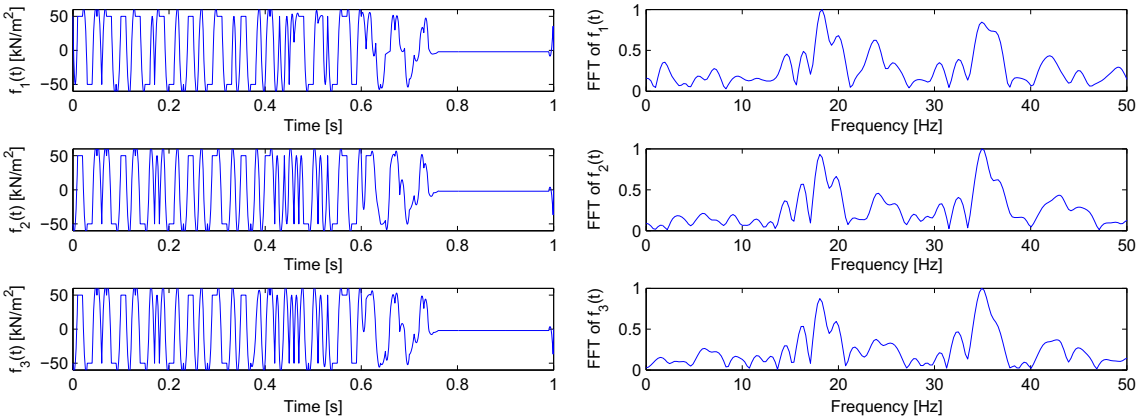

(a) Time signals (b) Frequency spectra

Fig. 13 Experiment 2—Time signals after optimization (time signal only)

in our experiment, the choice of time signals is not obvious from the frequency sweep results. A frequency sweep procedure, which is based on loading the entire surface of the (computational) domain, can become blind to the complex interference patterns created by waves emitted by a number of sources having finite widths. The degree of blindness depends, to a certain extent, on the heterogeneity of the geostructure. A frequency sweep procedure that involves using loads with smaller widths (e.g., 2 m) requires a combined frequency-and-location sweep, which is computationally expensive. These observations indicate the utility of the proposed inverse source approach in deciding the time signals driving wave sources used for focusing vibrational energy.

5.2 Experiment 2–Source location and signal optimization

In this experiment, we discuss the optimization of the wave sources' spatial and temporal characteristics. The time signal and load location optimization can be performed either sequentially or simultaneously. In a sequential process, the time signals are optimized first, without changing the load

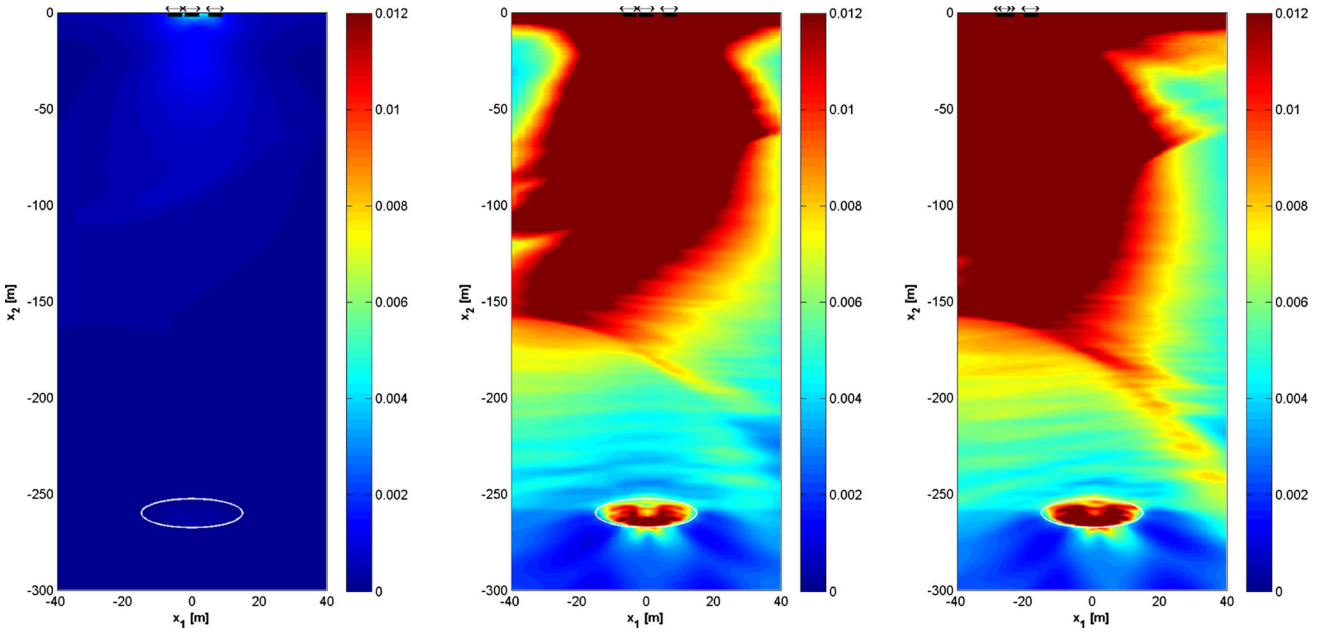

(a) KE_{TA} for the initial guess of time signals: loads located at (7,0)m, (-5,0)m, and (0,0)m

(b) KE_{TA} after time signal optimization: loads located at (7,0)m, (-5,0)m, and (0,0)m

(c) KE_{TA} after load location optimization: loads located at (-18.1,0)m, (-26.5,0)m, and (-25.2,0)m

Fig. 14 Experiment 2—Time-averaged kinetic energy (sequential optimization)

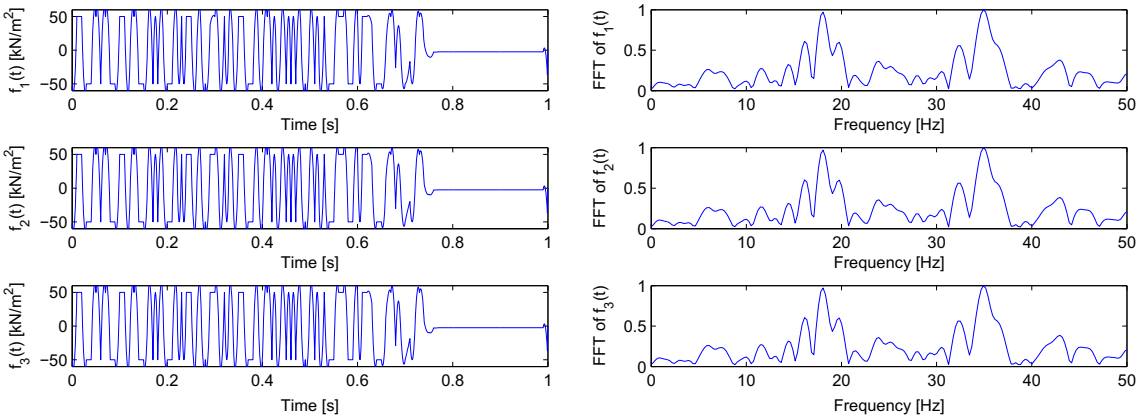

(a) Time signals (b) Frequency spectra

Fig. 15 Experiment 2—Time signals after simultaneous optimization

locations. The converged (optimized) signals are then used, while the source locations are optimized, until convergence is reached. By contrast, the simultaneous optimization process is initiated with guesses for both time signals and load locations, and both the spatial and temporal characteristics are updated during every inversion iteration until convergence is reached. In this experiment, we compare the performance of the optimization algorithm with that of the frequency sweep.

Sequential optimization: To test the performance of the sequential optimization procedure, we use three horizontal loads on the surface ($x_2 = 0$) of the geological formation model. We use Eq. 24 to describe the spatial variability of the surface tractions. The loads are centered at (7,0)m, (−5, 0)m, and (0,0)m, i.e., $\eta_1 = 7$m, $\eta_2 = -5$m, and $\eta_3 = 0$m in Eq. 24. The temporal optimization process is initiated with the time signals shown in Fig. 12. Their Fourier transforms (Fig. 12b) show the presence of a wide range

Fig. 16 Experiment 2—Time-averaged kinetic energy (simultaneous optimization)

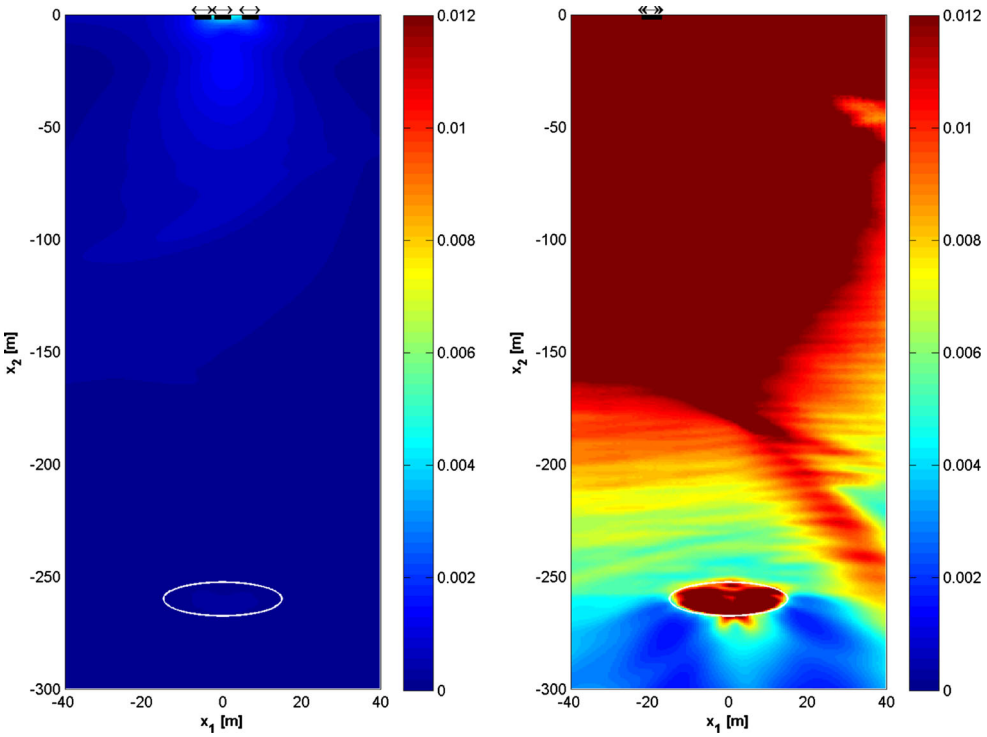

(a) KE_{TA} for the initial guess of time signals, loads located at (-5,0)m, (0,0)m, and (7,0)m

(b) KE_{TA} after time signal and load-location optimization, loads located at (-19,0)m, (-19.16,0)m, and (-20.04,0)m

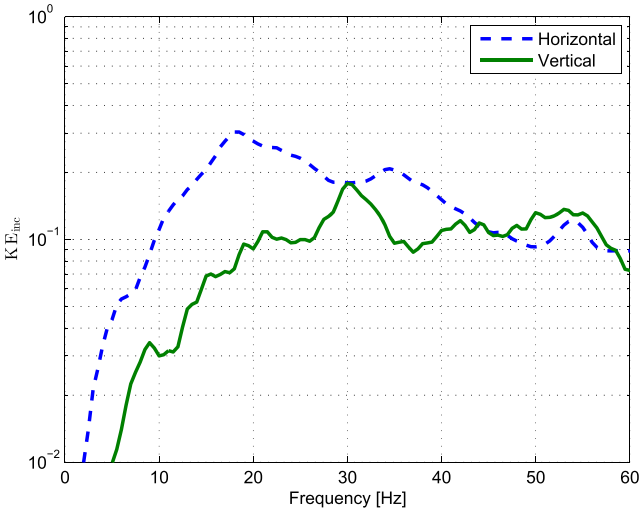

Fig. 17 Experiment 3—Frequency sweep results for vertical and horizontal loads

of frequencies. We, next, perform the time signal optimization using the DTO procedure. The optimizer converges to the time signals shown in Fig. 13. The plots for the time-averaged kinetic energy (KE_{TA}) for the initially guessed and for the converged time signals are compared in Fig. 14. KE_{inc} for the converged time signals is 3.22 J/m. A closer look at the frequency spectra of the converged time signals (Fig. 13b) reveals that the optimizer converged to signals with dominant frequencies at 18.3 and 34.5 Hz. Recall that these frequencies correspond to the minima revealed by the frequency sweep (Fig. 6).

Next, we carry out the optimization for the load locations. We use the converged time signals (Fig. 13) as fixed driving signals for the loads. We allow the optimizer to change the locations of loads in order to improve the energy delivery to the target inclusion. The loads move to the left and the converged locations are given by $(-18.1, 0)$m, $(-26.5, 0)$m, and $(-25.2, 0)$m. KE_{inc} at the end of sequential optimization is 3.85 J/m. The plot of time-averaged kinetic energy is shown in Fig. 14c. Note that the algorithm was able to deliver 20 % more energy merely by changing the locations of loads, i.e., by allowing the waves to constructively interfere in the target inclusion.

In the sequential optimization process, fixing the frequency content of time signals while searching for optimal locations may hinder the desired focusing. We have

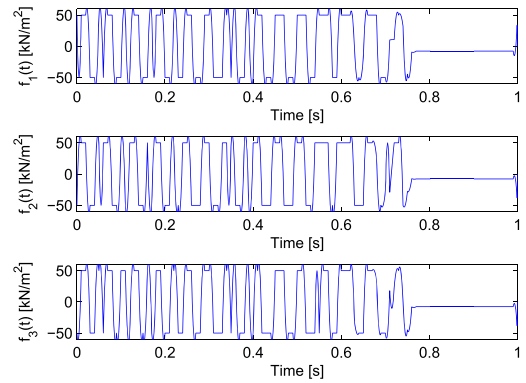

(a) Converged time signals - horizontal loads

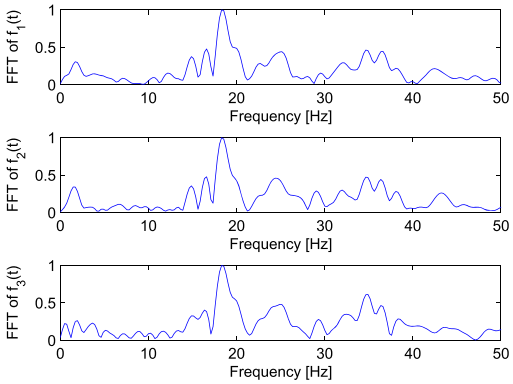

(b) Frequency spectra of converged time signals - horizontal loads

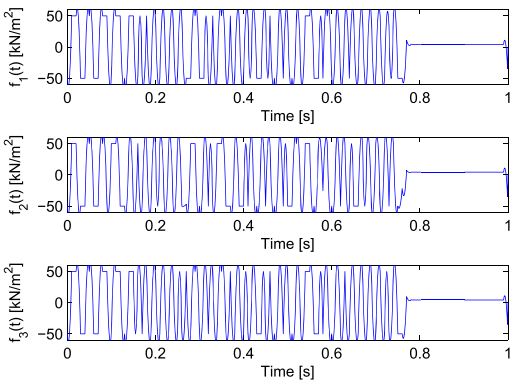

(c) Converged time signals - vertical loads

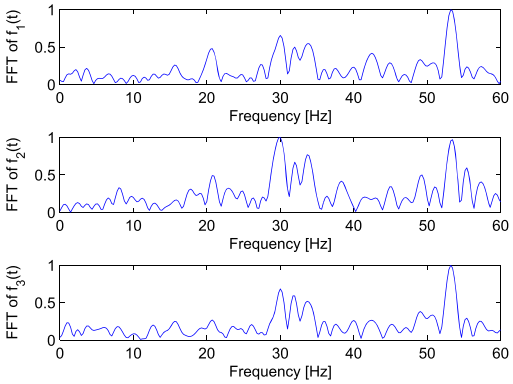

(d) Frequency spectra of converged time signals - vertical loads

Fig. 18 Experiment 3—Time signals and frequency spectra

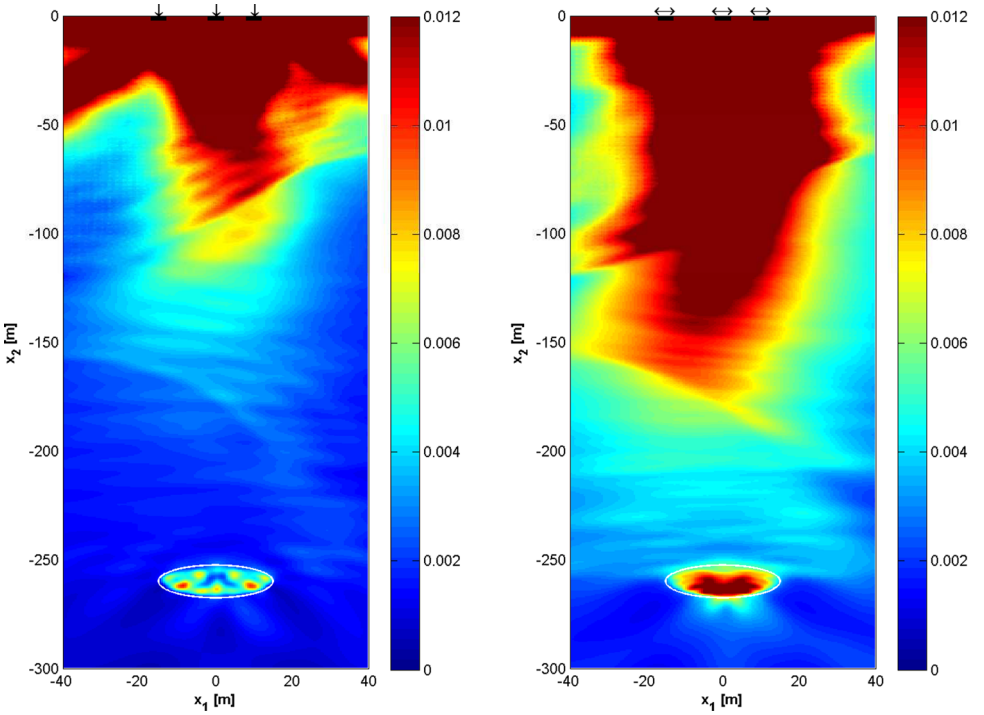

(a) $\mathrm{KE_{TA}}$ after time signal optimization - vertical loads located at (10,0)m, (-15,0)m, and (0,0)m

(b) $\mathrm{KE_{TA}}$ after time signal optimization - horizontal loads located at (10,0)m, (-15,0)m, and (0,0)m

Fig. 19 Experiment 3—Time-averaged kinetic energy

observed that the optimal frequency content of the sources depends on their location. To investigate this effect, we perform simultaneous optimization, which retains the flexibility of temporal and spatial characteristics during the entire inversion process.

Simultaneous optimization: We begin with an initial guess of time signals (Fig. 12), and load locations, which are the same as those used in the sequential optimization case, i.e., (7,0)m, $(-5, 0)$m, and (0,0)m). During each optimization iteration, we update the time signals, as well as the load locations, using the search direction for the respective control variable. The converged time signals are shown in Fig. 15, and the time-averaged kinetic energy is plotted in Fig. 16. Note that the converged frequency spectra for the loads in their optimized location (Fig. 15b) are different from those obtained based on time signal optimization for fixed load locations (Fig. 13b). The loads move to the left and the converged locations are $(-19, 0)$m, $(-19.16, 0)$m, and $(-20.04, 0)$m. $\mathrm{KE_{inc}}$ for the converged time signals and locations is 4.75 J/m, which is about 50 % higher than that achieved by performing time signal optimization with constant load locations (Fig. 14b), and about 23 % higher than that achieved by the sequential time signal and load location optimization (Fig. 14c).

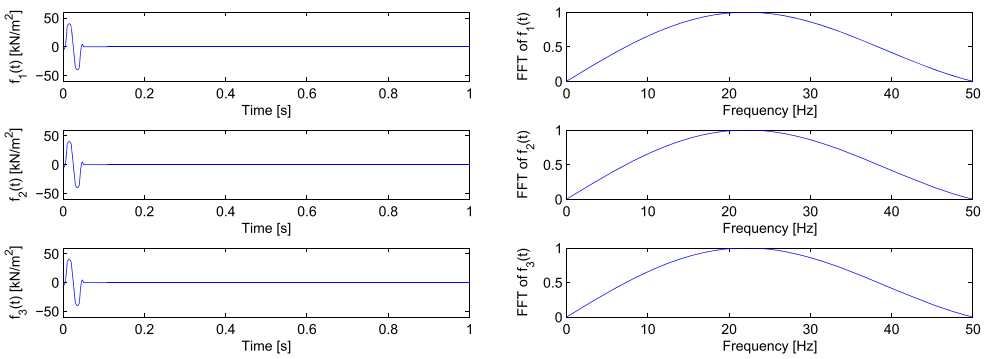

(a) Time signals

(b) Frequency spectra

Fig. 20 Experiment 4—Initial guess

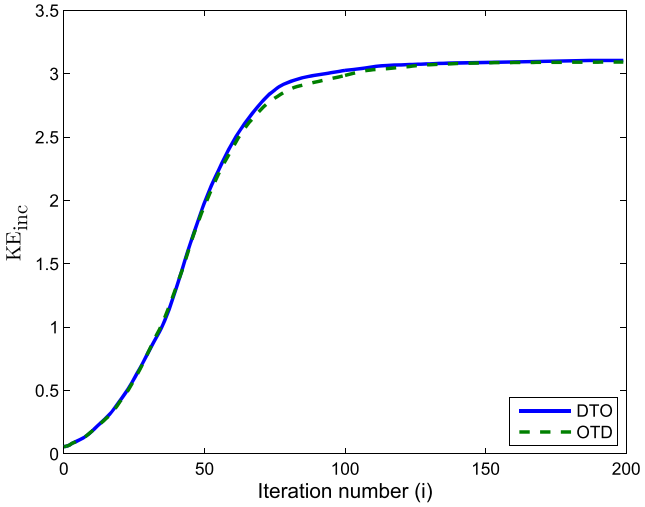

Fig. 21 Experiment 4—Growth of time-averaged kinetic energy for the inversion iterations

This experiment further highlights the importance of load location optimization: in the sequential optimization, we observed that about 20 % more energy can be delivered to the target formation by placing loads at advantageous locations. In the sequential optimization, the time signals are kept constant while performing load location optimization. Since the optimal frequency content of a load depends on its location, the sequential optimization cannot adequately compensate. The simultaneous optimization, on the other hand, is able to adjust both the temporal and spatial characteristics of loads and achieves (about 50 %) better energy delivery when compared to the time signal optimization.

5.3 Experiment 3—Polarization effect

Experiment 3 is designed to determine the effect of polarization of applied tractions on the wave energy focusing. Fundamental solutions for point loads on a (homogeneous) elastic halfspace [17] indicate that, for example, for a Poisson's ratio of 0.2, a horizontal load radiates about 50 % of the energy via P- and S-body waves. On the other hand, a vertical point load imparts about 70 % of its energy in the form of Rayleigh surface waves. Thus, for a homogeneous, elastic halfspace, horizontal (point) loads are more

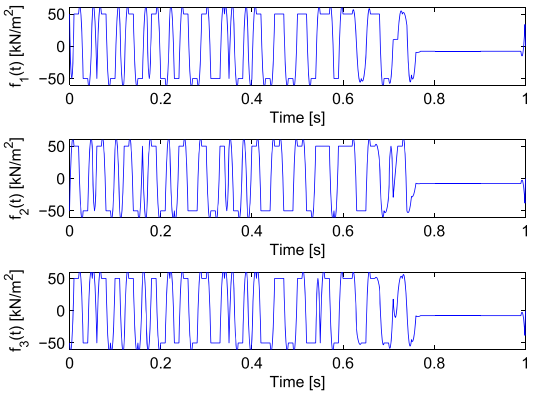

(a) Converged time signals (OTD)

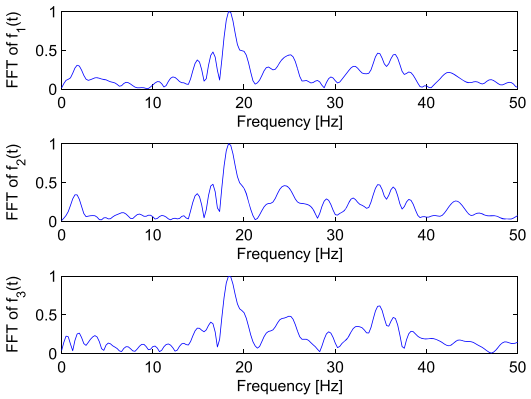

(b) Frequency spectra of converged time signals (OTD)

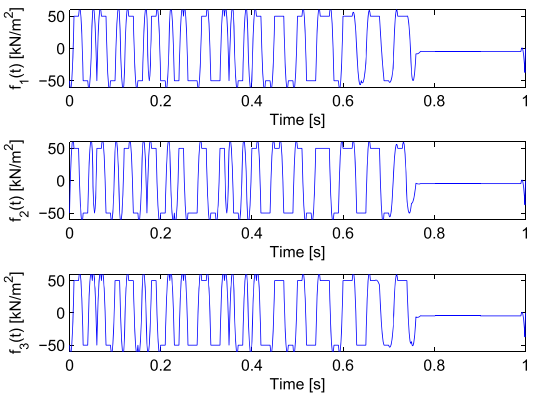

(c) Converged time signals (DTO)

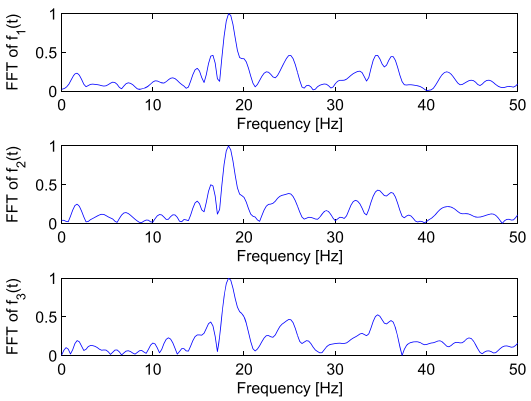

(d) Frequency spectra of converged time signals (DTO)

Fig. 22 Experiment 4—Time signals and frequency spectra

Fig. 23 Experiment 4—Time-averaged kinetic energy

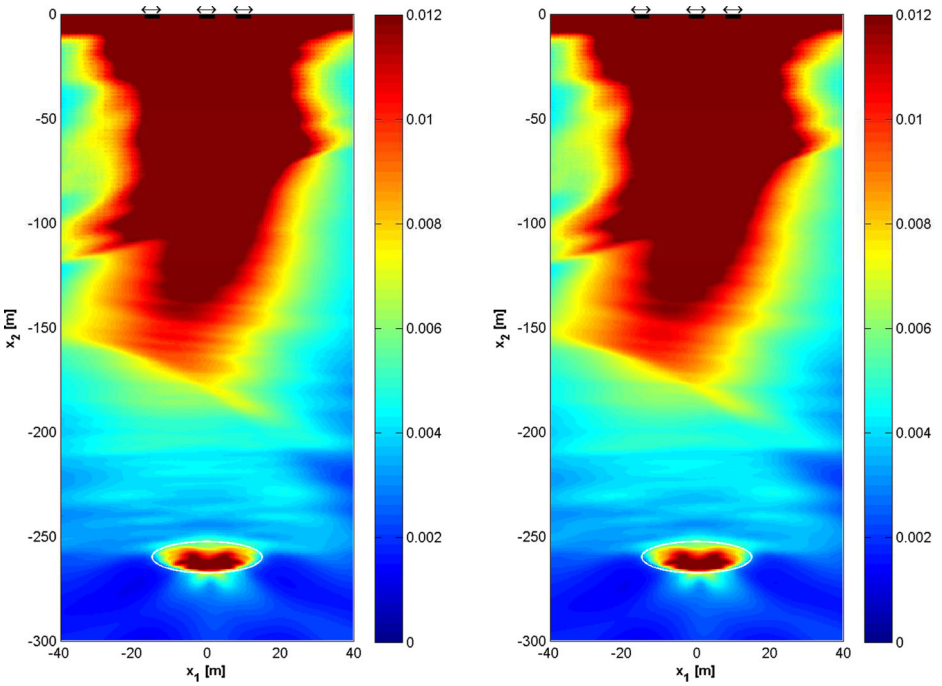

(a) KE_{TA} after time signal optimization - OTD, loads located at (-15,0)m, (0,0)m, and (10,0)m

(b) KE_{TA} after time signal optimization - DTO, loads located at (-15,0)m, (0,0)m, and (10,0)m

efficient at delivering energy to deeply situated subterranean formations. To capture the behavior for a heterogeneous halfspace excited by loads having finite widths, we plot the frequency sweep of KE_{inc} for horizontal and vertical loads (Fig. 17). Note that this is merely a different representation of the frequency sweeps reported earlier (Figs. 5 and 6). As seen in Fig. 17, the horizontally polarized load is able to deliver more vibrational energy to the target than the vertical load for a wide range of frequencies.

To further illustrate the effects of loading direction, we compare the results of time signal optimization performed with three horizontal and three vertical loads. The locations of the loads are kept constant. We use the OTD approach to carry out the time signal optimization. The initial guess of time signals for both the horizontally and vertically polarized loads is shown in Fig. 9. The loads are centered at (10,0)m, $(-15, 0)$m, and (0,0)m. We use Eq. 23 to specify the spatial variability of the loads. The converged time signals and their frequency content are depicted in Fig. 18. Figure 19 shows the plots of KE_{TA}. KE_{inc} for the vertical loads is 1.63 J/m (Fig. 19a), whereas that for the horizontal loads is 3.09 J/m (Fig. 19b), an almost twofold increase. Thus, our experiment indicates that horizontally polarized loads are able to deliver more vibrational energy.

Though, both theory and the numerical experiment reported herein suggest that horizontal loads are preferable for focusing, we note that our model does not account for intrinsic and/or apparent attenuation. A judicious choice about the preferred direction of loading can be made after considering the Q-factors for P and S waves in the geostructure of interest.

Table 2 "True" material properties for the geological formation model of Fig. 4

	C_p (m/s)	C_v (m/s)
Target inclusion	762	466
M1	953	583
M2	1204	737
M3	1394	853
M4	1685	1032

5.4 Experiment 4—OTD versus DTO

In this experiment, we use the same geological model to compare the performance of the OTD and DTO procedures. We carry out time signal optimization for three horizontal loads using both methods. The initial guess for the time signals is shown in Fig. 20.

Figure 21 shows that the DTO approach is able to deliver slightly more kinetic energy to the target in the time-averaged sense, but, in general, the differences are small. Nevertheless, in view of its ease of formulation and slightly better performance, we favor the DTO approach.

In Fig. 22, we compare the converged time signals, and Fig. 23 shows the time-averaged kinetic energy for the two procedures. Both procedures successfully recover the time signals, which exhibit a dominant frequency of, approximately, 18.3 Hz.

5.5 Experiment 5—The effect of formation property uncertainties on energy focusing

The working hypothesis of our theoretical development and of the preceding numerical experiments is that the material properties of the geological formation (Fig. 4) are known with confidence. However, in practice, precise knowledge of the properties of the geostructure is elusive. Though a systematic treatment of the effect property uncertainties may have on energy focusing escapes the scope of this communication, in this section, we briefly outline methodologies that would allow the formal treatment of uncertainties and could lead to the quantification of their effects on focusing.

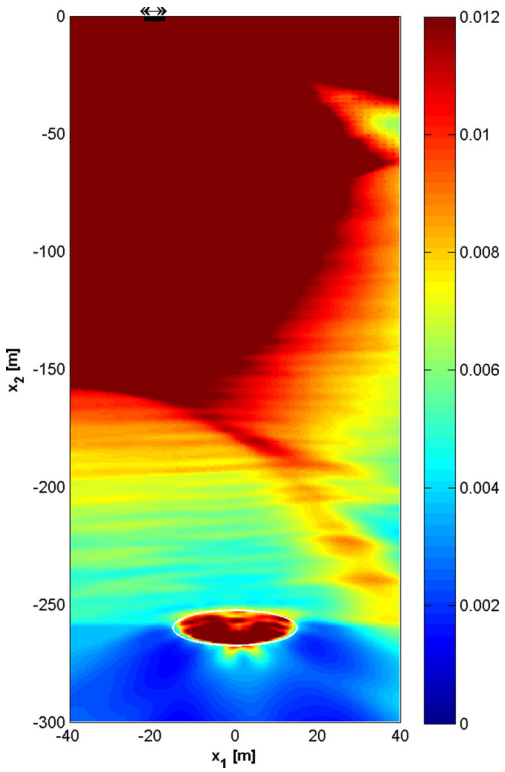

Fig. 24 Time-averaged kinetic energy for the geological formation with "true" material properties

The following simple numerical experiment highlights the issues: we first assume that the properties of the geological formation model depicted in Fig. 4 are inaccurate, and that the "true" properties are those given in Table 2, reflecting a 5 to 11 % change in the velocities compared to those in Fig. 4. Next, we are interested in quantifying the energy focusing when the "true" properties are used, while the formation is subjected to the optimal loads we obtained using the inaccurate wave velocity values. We are concerned with both the strength of the focusing, as well as with a potential shift to the focusing area. To this end, we use the spatio-temporally optimized loads obtained in Experiment 2 (Figs. 15 and 16) to excite the geological formation with the "true" properties as given in Table 2. The resulting distribution of $\mathrm{KE}_{\mathrm{TA}}$ is shown in Fig. 24. The resulting value of $\mathrm{KE}_{\mathrm{inc}}$ was reduced from 4.75 J/m (Experiment 2) to 4.11 J/m, a reduction of about 13 %.

It is clear that, while the material interfaces remained unaltered, a non-uniform increase in the properties of the formation led to a reduction of the strength of the focused energy, with no appreciable effects on the focusing area. The result is rather expected and warrants a formal treatment. We briefly outline two systematic approaches that could be used to quantify the effect of property uncertainties on the focusing.

– **Sensitivity analysis:** A sensitivity analysis of the elastodynamic system [19] can be carried out to quantify the dependence of $\mathrm{KE}_{\mathrm{inc}}$ on the material parameters. A first-order sensitivity analysis gives rise to a discrete forward problem (13) cast in terms of the unknown sensitivity variable $\mathbf{z}$, where $\mathbf{z} = \frac{\partial \mathbf{u}}{\partial q_1}$ and q_1 is the material parameter of interest (for example, $q_1 = \lambda_{\mathrm{b}_1}$–the first Lamé parameter of the top layer). The force vector for the sensitivity problem depends on the displacement, velocity, and acceleration fields ($\mathbf{u}$, $\dot{\mathbf{u}}$, $\ddot{\mathbf{u}}$), and the derivatives of the global system matrices with respect to q_1 ($\frac{\partial \mathbf{M}}{\partial q_1}$, $\frac{\partial \mathbf{C}}{\partial q_1}$, $\frac{\partial \mathbf{K}}{\partial q_1}$). Upon solution of the sensitivity problem, one recovers the time histories of the sensitivity variable and its time derivatives. The time histories can be used to calculate the derivative of $\mathrm{KE}_{\mathrm{inc}}$ with respect to q_1 ($\frac{\partial \mathrm{KE}_{\mathrm{inc}}}{\partial q_1}$). Thus, the analysis determines the

sensitivity of $\mathrm{KE_{inc}}$ to material parameters of various layers in the formation.

– **Reliability analysis:** In this approach, the material properties are treated as random variables endowed with suitable probability distribution functions (PDFs). The deterministic inverse source problem can be solved for the mean values of the material properties to arrive at the spatio-temporally optimal loads ($\mathbf{F}^{\mathrm{mean}}$). The time-averaged kinetic energy of the inclusion ($\mathrm{KE_{inc}}$) is also a random variable, and its value for the mean material properties and corresponding optimal loading ($\mathbf{F}^{\mathrm{mean}}$) can be computed as $\mathrm{KE}_{\mathrm{inc}}^{\mathrm{mean}}$. The probability of attaining a $\mathrm{KE_{inc}}$ value less than or equal to a predefined threshold $\delta\mathrm{KE}_{\mathrm{inc}}^{\mathrm{mean}}$ (where $0 < \delta < 1$), i.e., $\mathrm{P}[\mathrm{KE_{inc}} - \delta\mathrm{KE}_{\mathrm{inc}}^{\mathrm{mean}} \leq 0]$, when $\mathbf{F}^{\mathrm{mean}}$ is used as the surface excitation, can be evaluated using first-order reliability methods (FORM). The reliability analysis requires computation of derivatives of $\mathrm{KE_{inc}}$ with respect to various material parameters ($\frac{\partial \mathrm{KE_{inc}}}{\partial q_i}$), similarly to the sensitivity analysis. As explained above, it can be used to calculate the probability of failure in achieving a certain threshold $\mathrm{KE_{inc}}$, given the PDFs for the material parameters in the geostructure.

6 Conclusions

We presented an inverse source approach for focusing energy in a target subterranean formation and discussed two possible numerical implementations, DTO and OTD. Through numerical experiments, we provided evidence of the inverse source method's superiority over frequency sweeps for determining the optimal wave source locations and time signals. Moreover, the method's ability to resolve the optimal spatio-temporal characteristics of the wave source was shown to result in the strongest energy focusing among all studied alternatives. Our numerical experiments also indicate that horizontally polarized loads may be preferable over vertical loads. Lastly, we observed no significant performance difference between the two numerical implementations we discussed (DTO and OTD).

Acknowledgments The authors' work was partially supported by an Academic Alliance Excellence grant between the King Abdullah University of Science and Technology in Saudi Arabia (KAUST) and the University of Texas at Austin. The support is gratefully acknowledged.

Appendix: A Element matrices

Here, we present concise definitions of element matrices that form the global matrices in Eq. 10. A detailed description and definitions of parameters α_i $(i = 1, 2)$, β_i $(i = 1, 2)$, etc. can be found in [13].

$$D\mathbf{M}^{\mathrm{loc}} = \int_{\Omega_{\mathrm{loc}}} D\Phi\Phi^T d\Omega,\ D\mathbf{Q}_{ij}^{\mathrm{loc}} = \int_{\Omega_{\mathrm{loc}}} D\frac{\partial\Phi}{\partial x_i}\frac{\partial\Phi^T}{\partial x_j}d\Omega$$

$$\mathbf{A}_{ijk} = \int_{\Omega_{\mathrm{PML}}} i_j \frac{\partial\Phi}{\partial x_k}\Psi^T d\Omega\ \mathbf{F}^i = \int_{\Gamma_{\mathrm{load}}} \Phi^T f^i d\Gamma$$

$$\begin{aligned}\mathbf{N}_{ik} &= \int_{\Omega_{\mathrm{PML}}} k\frac{2\mu_{\mathrm{b}}+\lambda_{\mathrm{b}}}{4\mu_{\mathrm{b}}(\mu_{\mathrm{b}}+\lambda_{\mathrm{b}})}\Psi\Psi^T d\Omega, \qquad \text{if } i=1,\\ &= \int_{\Omega_{\mathrm{PML}}} k\frac{\lambda_{\mathrm{b}}}{4\mu_{\mathrm{b}}(\mu_{\mathrm{b}}+\lambda_{\mathrm{b}})}\Psi\Psi^T d\Omega, \qquad \text{if } i=2,\\ &= \int_{\Omega_{\mathrm{PML}}} k\frac{1}{2\mu_{\mathrm{b}}}\Psi\Psi^T d\Omega, \qquad \text{if } i=3,\end{aligned}$$

For a finite element within the target inclusion, the element mass, damping, and stiffness matrices are given by:

$$\mathbf{M}_{\mathrm{a}} = \begin{bmatrix}\rho_{\mathrm{a}}\mathbf{M}^{\mathrm{a}} & 0\\ 0 & \rho_{\mathrm{a}}\mathbf{M}^{\mathrm{a}}\end{bmatrix}, \mathbf{C}_{\mathrm{a}} = \begin{bmatrix}0\ 0\\ 0\ 0\end{bmatrix},$$

$$\mathbf{K}_{\mathrm{a}} = \begin{bmatrix}(2\mu_{\mathrm{a}}+\lambda_{\mathrm{a}})\,\mathbf{Q}_{11}^{\mathrm{a}}+\mu_{\mathrm{a}}\mathbf{Q}_{22}^{\mathrm{a}} & \mu_{\mathrm{a}}\mathbf{Q}_{21}^{\mathrm{a}}+\lambda_{\mathrm{a}}\mathbf{Q}_{12}^{\mathrm{a}}\\ \mu_{\mathrm{a}}\mathbf{Q}_{12}^{\mathrm{a}}+\lambda_{\mathrm{a}}\mathbf{Q}_{21}^{\mathrm{a}} & (2\mu_{\mathrm{a}}+\lambda_{\mathrm{a}})\mathbf{Q}_{22}^{\mathrm{a}}+\mu_{\mathrm{a}}\mathbf{Q}_{11}^{\mathrm{a}}\end{bmatrix}.$$

Element matrices for the regular domain are:

$$\mathbf{M}_{\mathrm{reg}} = \begin{bmatrix}\rho_{\mathrm{b}}\mathbf{M}^{\mathrm{reg}} & 0\\ 0 & \rho_{\mathrm{b}}\mathbf{M}^{\mathrm{reg}}\end{bmatrix}, \mathbf{C}_{\mathrm{reg}} = \begin{bmatrix}0\ 0\\ 0\ 0\end{bmatrix},$$

$$\mathbf{K}_{\mathrm{reg}} = \begin{bmatrix}(2\mu_{\mathrm{b}}+\lambda_{\mathrm{b}})\,\mathbf{Q}_{11}^{\mathrm{reg}}+\mu_{\mathrm{b}}\mathbf{Q}_{22}^{\mathrm{reg}} & \mu_{\mathrm{b}}\mathbf{Q}_{21}^{\mathrm{reg}}+\lambda_{\mathrm{b}}\mathbf{Q}_{12}^{\mathrm{reg}}\\ \mu_{\mathrm{b}}\mathbf{Q}_{12}^{\mathrm{reg}}+\lambda_{\mathrm{b}}\mathbf{Q}_{21}^{\mathrm{reg}} & (2\mu_{\mathrm{b}}+\lambda_{\mathrm{b}})\,\mathbf{Q}_{22}^{\mathrm{reg}}+\mu_{\mathrm{b}}\mathbf{Q}_{11}^{\mathrm{reg}}\end{bmatrix}.$$

In the PML region, the element matrices can be computed as:

$$\mathbf{M}_{\mathrm{PML}} = \begin{bmatrix}\rho_{\mathrm{b}}\mathbf{a}\mathbf{M}^{\mathrm{PML}} & 0 & 0 & 0 & 0\\ 0 & \rho_{\mathrm{b}}\mathbf{a}\mathbf{M}^{\mathrm{PML}} & 0 & 0 & 0\\ 0 & 0 & -\mathbf{N}_{1\mathrm{a}} & \mathbf{N}_{2\mathrm{a}} & 0\\ 0 & 0 & \mathbf{N}_{2\mathrm{a}} & -\mathbf{N}_{1\mathrm{a}} & 0\\ 0 & 0 & 0 & 0 & -\mathbf{N}_{3\mathrm{a}}\end{bmatrix},$$

$$\mathbf{C}_{\mathrm{PML}} = \begin{bmatrix}\rho_{\mathrm{b}}\mathbf{b}\mathbf{M}^{\mathrm{PML}} & 0 & \mathbf{A}_{\alpha 21} & 0 & \mathbf{A}_{\alpha 12}\\ 0 & \rho_{\mathrm{b}}\mathbf{b}\mathbf{M}^{\mathrm{PML}} & 0 & \mathbf{A}_{\alpha 12} & \mathbf{A}_{\alpha 21}\\ \mathbf{A}_{\alpha 21} & 0 & -\mathbf{N}_{1\mathrm{b}} & \mathbf{N}_{2\mathrm{b}} & 0\\ 0 & \mathbf{A}_{\alpha 12} & \mathbf{N}_{2\mathrm{b}} & -\mathbf{N}_{1\mathrm{b}} & 0\\ \mathbf{A}_{\alpha 12} & \mathbf{A}_{\alpha 21} & 0 & 0 & -\mathbf{N}_{3\mathrm{b}}\end{bmatrix},$$

$$\mathbf{K}_{\mathrm{PML}} = \begin{bmatrix}\rho_{\mathrm{b}}\mathbf{c}\mathbf{M}^{\mathrm{PML}} & 0 & \mathbf{A}_{\beta 21} & 0 & \mathbf{A}_{\beta 12}\\ 0 & \rho_{\mathrm{b}}\mathbf{c}\mathbf{M}^{\mathrm{PML}} & 0 & \mathbf{A}_{\beta 12} & \mathbf{A}_{\beta 21}\\ \mathbf{A}_{\beta 21} & 0 & -\mathbf{N}_{1\mathrm{c}} & \mathbf{N}_{2\mathrm{c}} & 0\\ 0 & \mathbf{A}_{\beta 12} & \mathbf{N}_{2\mathrm{c}} & -\mathbf{N}_{1\mathrm{c}} & 0\\ \mathbf{A}_{\beta 12} & \mathbf{A}_{\beta 21} & 0 & 0 & -\mathbf{N}_{3\mathrm{c}}\end{bmatrix}.$$

Appendix: B Control problem derivations

Optimize-then-discretize approach

Time-signal optimization

We take the variation of the Lagrangian with respect to discrete scalar variables ξ_{mn} to obtain the gradient of $\mathcal{A}$, i.e.,

$$\delta_{(\xi_{ij})}\mathcal{A} = \nabla_{(\xi_{ij})}\mathcal{A} = -\int_{\Gamma_{\text{load}}}\int_0^T \boldsymbol{\lambda}_F \cdot \frac{\partial \mathbf{f}}{\partial \xi_{ij}} dt\ d\Gamma, \text{ or,}$$

$$\begin{aligned}\nabla_{(\xi_{ij}=\xi_{mn})}\mathcal{A} &= -\frac{\partial}{\partial \xi_{mn}}\left[\sum_{i=1}^{n_s}\int_{\Gamma_{\text{load}}}\int_0^T \begin{bmatrix}\boldsymbol{\lambda}_{F1}(\mathbf{x})\\ \boldsymbol{\lambda}_{F2}(\mathbf{x})\end{bmatrix}\cdot \begin{bmatrix}\theta_{i1}(\mathbf{x})\\ \theta_{i2}(\mathbf{x})\end{bmatrix}\sum_{j=1}^{n_f}\xi_{ij}\tau_j(t)dt\ d\Gamma\right]\\ &= \int_{\Gamma_{\text{load}}}\int_0^T \begin{bmatrix}\boldsymbol{\lambda}_{u_{b_1}}(\mathbf{x})\\ \boldsymbol{\lambda}_{u_{b_2}}(\mathbf{x})\end{bmatrix}\cdot\begin{bmatrix}\theta_{m1}(\mathbf{x})\\ \theta_{m2}(\mathbf{x})\end{bmatrix}\tau_n(t)dt\ d\Gamma\\ &= \int_{\Gamma_{\text{load}}}\begin{bmatrix}\theta_{m1}(\mathbf{x})\Phi\\ \theta_{m2}(\mathbf{x})\Phi\end{bmatrix}\cdot\left(\int_0^T\begin{bmatrix}\boldsymbol{\lambda}_{u_{b_1}}(t)\\ \boldsymbol{\lambda}_{u_{b_2}}(t)\end{bmatrix}\tau_n(t)dt\right)d\Gamma.\end{aligned}$$

Load-location optimization

Variation of $\mathcal{A}$ with respect to the control parameter $\boldsymbol{\eta}$ is given by

$$\begin{aligned}\delta_{(\eta_m)}\mathcal{A} &= \nabla_{(\eta_m)}\mathcal{A}\\ &= -\int_{\Gamma_{\text{load}}}\int_0^T \boldsymbol{\lambda}_F\cdot\frac{\partial \mathbf{f}}{\partial \eta_m}dt\ d\Gamma\\ &= \int_{\Gamma_{\text{load}}}\frac{\partial\theta_{mk}(\mathbf{x})}{\partial\eta_m}\Phi^T\int_0^T\boldsymbol{\lambda}_{u_bk}(t)\sum_{j=1}^{n_f}\xi_{mj}\tau_j(t)dtd\Gamma.\end{aligned}$$

Discretize-then-optimize approach

Time-signal optimization

For any given nodal-excitation parameter ξ_{mn}, we get

$$\frac{\partial \mathcal{A}_d}{\partial \xi_{mn}} = \sum_{i=0}^{N}\ddot{\boldsymbol{\lambda}}_i^T\frac{\partial \mathbf{F}_i}{\partial \xi_{mn}}.$$

We recall that for each element

$$\begin{aligned}\mathbf{F}_k^{\text{elem}} &= \begin{bmatrix}\mathbf{F}_{k,x_1}^{\text{elem}}\\ \mathbf{F}_{k,x_2}^{\text{elem}}\end{bmatrix} = \sum_{i=1}^{n_s}\int_{\Gamma_{\text{load}}}\begin{bmatrix}\theta_{i1}(\mathbf{x})\Phi\\ \theta_{i2}(\mathbf{x})\Phi\end{bmatrix}\sum_{j=1}^{n_f}\xi_{ij}\tau_j(k\Delta t)\ d\Gamma,\\ \frac{\partial\mathbf{F}_k^{\text{elem}}}{\partial\xi_{mn}} &= \int_{\Gamma_{\text{load}}}\begin{bmatrix}\theta_{m1}(\mathbf{x})\Phi\\ \theta_{m2}(\mathbf{x})\Phi\end{bmatrix}\tau_n(k\cdot\Delta t)\ d\Gamma,\\ \sum_{k=0}^{N}\ddot{\boldsymbol{\lambda}}_k^T\frac{\partial\mathbf{F}_k^{\text{elem}}}{\partial\xi_{mn}} &= \sum_{k=0}^{N}\ddot{\boldsymbol{\lambda}}_{k,\text{load}}^T\int_{\Gamma_{\text{load}}}\begin{bmatrix}\theta_{m1}(\mathbf{x})\Phi\\ \theta_{m2}(\mathbf{x})\Phi\end{bmatrix}\tau_n(k\Delta t)\,d\Gamma,\end{aligned}$$

where $\ddot{\boldsymbol{\lambda}}_{k,\text{load}}$ contains the values of adjoint variable corresponding to the degrees of freedom represented by rows of vector Φ on Γ_{load}.

Load-location optimization

For a given load-location parameter η_m, we get

$$\frac{\partial \mathcal{A}_d}{\partial \eta_m} = \sum_{i=0}^{N}\ddot{\boldsymbol{\lambda}}_i^T\frac{\partial \mathbf{F}_i}{\partial \eta_m}.$$

For each loaded element,

$$\begin{aligned}\mathbf{F}_k^{\text{elem}} &= \begin{bmatrix}\mathbf{F}_{k,x_1}^{\text{elem}}\\ \mathbf{F}_{k,x_2}^{\text{elem}}\end{bmatrix} = \sum_{i=1}^{n_s}\int_{\Gamma_{\text{load}}}\begin{bmatrix}\theta_{i1}(\mathbf{x},\eta_i)\Phi\\ \theta_{i2}(\mathbf{x},\eta_i)\Phi\end{bmatrix}\cdot\sum_{j=1}^{n_f}\xi_{ij}\tau_j(k\Delta t)\ d\Gamma,\\ \frac{\partial\mathbf{F}_k^{\text{elem}}}{\partial\eta_m} &= \int_{\Gamma_{\text{load}}}\begin{bmatrix}\frac{\partial\theta_{m1}(\mathbf{x},\eta_m)}{\partial\eta_m}\Phi\\ \frac{\partial\theta_{m2}(\mathbf{x},\eta_m)}{\partial\eta_m}\Phi\end{bmatrix}\sum_{j=1}^{n_f}\xi_{mj}\tau_j(k\Delta t)\ d\Gamma,\\ \sum_{k=0}^{N}\ddot{\boldsymbol{\lambda}}_k^T\frac{\partial\mathbf{F}_k^{\text{elem}}}{\partial\eta_m} &= \sum_{k=0}^{N}\ddot{\boldsymbol{\lambda}}_{k,\text{load}}^T\int_{\Gamma_{\text{load}}}\begin{bmatrix}\frac{\partial\theta_{m1}(\mathbf{x},\eta_m)}{\partial\eta_m}\Phi\\ \frac{\partial\theta_{m2}(\mathbf{x},\eta_m)}{\partial\eta_m}\Phi\end{bmatrix}\cdot\sum_{j=1}^{n_f}\xi_{mj}\tau_j(k\Delta t)\ d\Gamma,\end{aligned}$$

where $\ddot{\boldsymbol{\lambda}}_{k,\text{load}}$ contains the values of adjoint variable corresponding to the degrees of freedom represented by rows of vector Φ on Γ_{load}.

References

1. Bamberger, A., Chavent, G., Lailly, P.: About the stability of the inverse problem in 1-D wave equations application to the interpretation of seismic profiles. Appl. Math. Optim. **5**(1), 1–47 (1979)
2. Beresnev, I., Gaul, W., Vigil, R.D.: Direct pore-level observation of permeability increase in two-phase flow by shaking. Geophys. Res. Lett. **38**(20) (2011). doi:10.1029/2011GL048840
3. Beresnev, I.A., Deng, W.: Viscosity effects in vibratory mobilization of residual oil. Geophys. **4**, N79–N85 (2010)
4. Beresnev, I.A., Johnson, P.A.: Elastic-wave stimulation of oil production: a review of methods and results. Geophys. **59**(6), 1000–1017 (1994)
5. Bunks, C., Saleck, F., Zaleski, S., Chavent, G.: Multiscale seismic waveform inversion. Geophys. **60**(5), 1457–1473 (1995)
6. Deng, W., Cardenas, M.B.: Dynamics and dislodgment from pore constrictions of a trapped nonwetting droplet stimulated by seismic waves. Water Res. Res. **49**(7), 4206–4218 (2013)
7. Epanomeritakis, I., Akçelik, V., Ghattas, O., Bielak, J.: A Newton-CG method for large-scale three-dimensional elastic full-waveform seismic inversion. Inverse Problems **24**(3), 034,015 (2008)
8. Gunzburger, M.D.: Perspectives in flow control and optimization SIAM (2003)
9. Jeong, C., Kallivokas, L.F., Huh, C., Lake, L.W.: Optimization of sources for focusing wave energy in targeted formations. J. Geophys. Eng. **7**(3), 242 (2010)

10. Jeong, C., Kallivokas, L.F., Huh, C., Lake, L.W.: Maximization of oil mobility within a hydrocarbon reservoir for elastic wave-based enhanced oil recovery, In: SPE Annual Technical Conference and Exhibition, SPE 147150. Society of Petroleum Engineers (2011)
11. Kallivokas, L., Fathi, A., Kucukcoban, S., Stokoe(II), K., Bielak, J., Ghattas, O.: Site characterization using full waveform inversion. Soil Dyn. Earthquake Eng. **47**, 62–82 (2013)
12. Kostrov, S.A., Wooden, B.O.: Mechanisms, field suitability, and case studies for enhancement of oil recovery and production using in-situ seismic stimulation. In: 16th International Symposium on Nonlinear Acoustics (2002)
13. Kucukcoban, S., Kallivokas, L.: A symmetric hybrid formulation for transient wave simulations in pml-truncated heterogeneous media. Wave Motion **50**(1), 57–79 (2013)
14. Lake, L.: Enhanced Oil Recovery Prentice Hall Incorporated (1989)
15. Petra, N., Stadler, G.: Model variational inverse problems governed by partial differential equations. Tech. Rep. 11-5, The Institute for Computational Engineering and Sciences, The University of Texas at Austin (2011)
16. Roberts, P.M., Majer, E.L., Lo, W.C., Sposito, G., Daley, T.M.: An integrated approach to seismic stimulation of oil reservoirs: Laboratory, field and theoretical results from doe/industry collaborations. In: 16th International Symposium on Nonlinear Acoustics (2002)
17. Sánchez-Sesma, F.J., Weaver, R.L., Kawase, H., Matsushima, S., Luzón, F., Campillo, M.: Energy partitions among elastic waves for dynamic surface loads in a semi-infinite solid. Bulletin of the Seismological Society of America **101**(4), 1704–1709 (2011)
18. Tarantola, A.: Inversion of seismic reflection data in the acoustic approximation. Geophys. **49**(8), 1259–1266 (1984)
19. Tsikas, A.: Sensitivity analysis of elastodynamic systems. Master's thesis, Department of Civil and Environmental Engineering, Carnegie Mellon University (1997)